



City Research Online

City, University of London Institutional Repository

Citation: Corfar, D. A. & Tsavdaridis, K. (2024). Testing Novel Hybrid Inter-Module Joints for Steel Modular Buildings Under Cyclic Load. *Engineering structures*, 315, 118495. doi: 10.1016/j.engstruct.2024.118495

This is the accepted version of the paper.

This version of the publication may differ from the final published version.

Permanent repository link: <https://openaccess.city.ac.uk/id/eprint/33237/>

Link to published version: <https://doi.org/10.1016/j.engstruct.2024.118495>

Copyright: City Research Online aims to make research outputs of City, University of London available to a wider audience. Copyright and Moral Rights remain with the author(s) and/or copyright holders. URLs from City Research Online may be freely distributed and linked to.

Reuse: Copies of full items can be used for personal research or study, educational, or not-for-profit purposes without prior permission or charge. Provided that the authors, title and full bibliographic details are credited, a hyperlink and/or URL is given for the original metadata page and the content is not changed in any way.

City Research Online:

<http://openaccess.city.ac.uk/>

publications@city.ac.uk



Testing novel hybrid inter-module joints for steel modular buildings under cyclic load

Dan-Adrian Corfar^a and Konstantinos Daniel Tsavdaridis^b

^{a,b} Department of Engineering, School of Science & Technology, City, University of London, EC1V 0HB, London, UK

*Corresponding author: Konstantinos.Tsavdaridis@city.ac.uk

Abstract. To bridge the gap between the unrealised disassembly and reuse potential of volumetric modular buildings and the lack for seismic resilience, a hybrid inter-module connection employing a high-damping rubber bearing was proposed to reduce the inelastic deformation in the members of the volumetric module. The cyclic behaviour of the proposed connection was previously investigated at connection level through validated proof-of-concept FEA, reflecting promising damping and re-centring capabilities. In this study, six in-plane cyclic loading tests on inter-module joints with the novel, hybrid inter-module connection were carried out to investigate the connection's influence on the cyclic behaviour of steel modular buildings under lateral load at joint level. The tests focused on the contribution of the laminated elastomeric bearing to the joint's lateral behaviour and the effect of different bolting assemblies on the working mechanism of the hybrid connection system. The standard FEMA/SAC loading sequence was employed on single-span, meso-scale joint prototypes with axial and in-plane lateral loading applied to the top post. The results showed that the hybrid IMJs exhibited nonlinear, multi-stage hysteretic responses, governed by the bending resistance of the bolting assembly and the stiffness of the intra-module connection. The aseismic performance of the joints was characterised by residual drifts below the permissible limit of 0.5% up to 2% drift ratio and high equivalent viscous damping during the low-amplitude cycles. Overall, the tests demonstrated the feasibility of the proposed connection with respect to the mitigation of damage in the structural elements of the volumetric modules after an earthquake, as proved by the low inelastic deformation recorded up to 4% drift ratios.

Keywords: high-damping rubber, inter-module connections, seismic behaviour, shape-memory alloy, steel modular buildings



1. Introduction

In view of the ongoing climate emergency and exacerbating housing crisis around the globe, the United Nations' Sustainable Development Goals have accentuated the need to embrace sustainability and resilience in the planning and design of urban landscapes [1].

In the last decade, the rapid technological advancements in modern methods of construction (MMC) have reinforced the sustainability benefits of prefabrication, standardisation, and lean design with regard to resource efficiency and reduced waste [2–5]. Furthermore, with circular design principles such as Design for Manufacture and Assembly (DfMA) and Design for Deconstruction (DfD) at the core of volumetric modular construction, steel Modular Building Systems (MBSs) have been regarded as a compelling solution that would help accelerate the transition to a circular economy in the built environment [6–9].

Completing the SDGs narrative from a seismic-resistant perspective, the resilience of a building can be conveyed by its ability to meet performance objectives such as functional recovery on top of safety, motivated by the desire to minimise the major disruption and financial losses associated with severe damage to the building's structure in the aftermath of an earthquake. Meanwhile, the ever-increasing height of self-standing steel MBSs in the world's megacities has drawn a lot of attention to the critical role of the inter-module connections (IMCs) to the global structural response of steel modular buildings under lateral load [10–14]. The design of IMCs is also paramount for the ease of disassembly and adaptability of steel MBSs, yet current practice often compromises on demountability in favour of frame continuity by adopting welded or grouted joints between modules [15]. At the same time, significant effort has been devoted to adopting capacity-based design principles from traditional steel moment resisting frames (MRFs) in steel MBSs and design inter-module joints to perform elastically, while plastic hinges would be concentrated in the beams of the module [16–19]. Although effective for the goal of overall safety, this design paradigm results in large residual deformation, reducing the functionality and ease of disassembly of the steel MBSs, while the permanent damage to the volumetric unit renders its reusability impractical.

Thus, when resources allow more expensive goals such as post-earthquake functionality to be considered in the design of steel modular buildings under lateral load, it becomes highly desirable to avoid damaging the structural framing of the module in order to meet the functional objective and improve the seismic resilience of the modular building stock



while also facilitating the disassembly and reuse of the volumetric module. Moreover, given the discretised nature of volumetric modular buildings with multiple, repetitive connection points at the interfaces of stacked or adjacent modules, there is ample scope in aiming to spread the efforts developed under lateral load throughout the building by engaging the numerous inter-module connections more effectively in the global damage distribution mechanism. In this regard, there has been increasing interest among researchers to enhance the mechanical response of IMCs by exploiting various energy-dissipating and self-centring parts [20–26]. In a recent study [27], the authors have introduced a novel hybrid IMC made with high-damping rubber (HDR) and superelastic shape-memory alloy (SMA) parts, developed to reduce the permanent damage in the members of the volumetric module. While the proof-of-concept finite element analysis (FEA) study has reflected a favourable cyclic behaviour of the hybrid IMC at the material (micro-) and connection component (small-scale) level, experimental evidence is necessary to gain further insights into the force-transfer mechanism and cyclic performance of the novel connection from a joint (meso-) and frame (large-scale) level perspective.

In this study, a series of tests has been carried out to determine the feasibility of the proposed connection at joint level, by investigating the in-plane cyclic lateral behaviour of inter-module joints (IMJs) equipped with the hybrid IMC. The tests simulated the effect of gravitational and cyclic lateral load on single-span, meso-scale joint assemblies with full-size members, considering the influence of the material and size of the bolting assemblies as well as the intra-module connection stiffness on the mechanical response of the hybrid IMJ prototypes.

2. Configuration of the novel hybrid IMC

The proposed connection has been designed to fulfil the essential functions of vertical and horizontal connectivity between modules, while the centred alignment of the member cross-sections to the box corners eliminates the unfavourable effect of eccentric loads caused by offsets. A corner inter-module joint equipped with the novel, hybrid IMC consists of a laminated elastomeric bearing (LEB) clamped between steel box corner fittings by means of a bolting assembly (Fig. 1). The size of the box corners was restricted to that of the connecting frame members with a flush finish to allow a tight fit between members at external or internal joints where more than two modules come together, without increasing the horizontal gap between modules which would act adversely to the stiffness of the structure. While the straightforward installation sequence in Fig. 1



illustrates the assembly-friendly design of the IMC, the connection would still require working at height to install bolt assemblies, which should be accounted for in the method statement and risk assessment of the construction project. Among other prospective limitations of the proposed connection system, the presence of the rubber bearings in the joint may increase the design effort compared to simpler connections, particularly as it requires due consideration of the staged construction process to control the compression in the rubber layers as the building is erected.

Axial compression is transferred between the corner posts through the laminated elastomeric bearing made with steel reinforcing plates to control the level of vertical displacement, whereas tensile axial force is resisted by the bolting assembly. Horizontal shear forces are transferred through a combined mechanism of friction between the faying steel surfaces, shear resistance of the interlocking pins, rubber layers, and bending resistance of the bolt rod, while the interlocking pins also prevent accidental sliding.

To improve the energy dissipation capacity of the connection, the bearing has been fabricated with filled (high-damping) rubber instead of low-damping (unfilled) rubber, as the presence of high percentages of carbon black filler in HDR results in a much more pronounced hysteresis at the lower working shear strain levels (in the range of 50%-100%) due to the breakdown of carbon filler chain networks [28]. By comparison, unfilled (low-damping) rubber typically exhibits hysteresis due to strain-crystallisation at much larger extensions. Moreover, filled (high-damping) rubber shows a higher initial shear stiffness, ensuring that the IMC is not easily excited during more frequent low-magnitude seismic events or common low-intensity wind loads, reserving the available supplemental damping for stronger lateral loads.

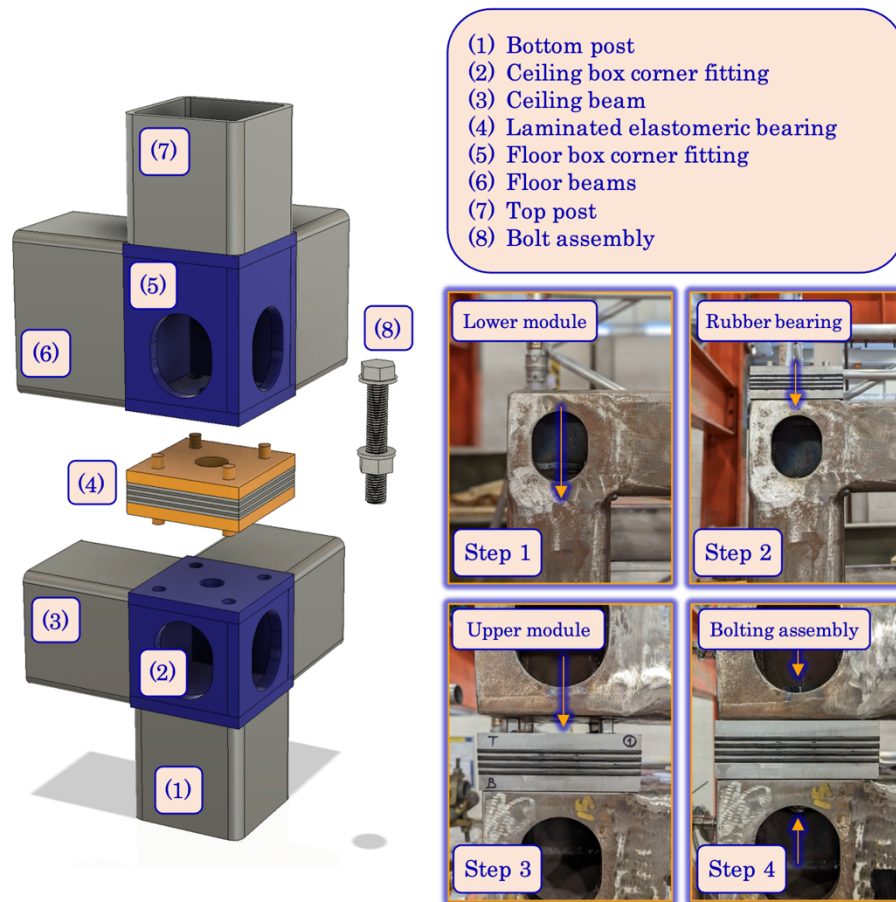


Fig. 1. Conceptual representation of the hybrid inter-module connection.

3. Cyclic loading tests

3.1. Test samples

The test IMJ prototypes were made of top and bottom beam-column subassemblies, and the inter-module connection between them. The meso-scale configuration (Fig. 2) was adopted as a cost-effective solution that replicates the deformed shape and anticipated points of inflection in planar modular frames subjected to in-plane lateral loads by taking the lengths of the posts and beams as half of those in the full-size frame panel.

The tests focused on the influence of six parameters on the mechanical behaviour of the hybrid IMJ prototypes (Table 1). Two sizes of austenitic shape-memory alloy (SMA) studs were considered to determine whether the nonlinearity associated with the phase transformation of superelastic Ni-Ti alloy has a meaningful effect on the re-centring and energy dissipation capacity of the joints. Likewise, high-strength steel bolts were adopted to allow for a direct comparison with the SMA studs, further highlighting the contribution of the size and material strength of the bolting assembly to the working mechanism of the connection. Also, two details of beam-column joints were employed to determine the role

of the intra-module connection's stiffness at joint level. Finally, it is worth mentioning that the six tests were carried out using only three joint assemblies and rubber bearings by re-testing prototype IMJ01 as IMJ03 and then again as IMJ04, while IMJ02 was re-tested as IMJ06. This decision was supported by the strain gauge readings which showed that the performance of the steel frames during the tests with SMA studs was essentially elastic, allowing for the reuse of the steel frames and bearings by just replacing the bolting assembly.

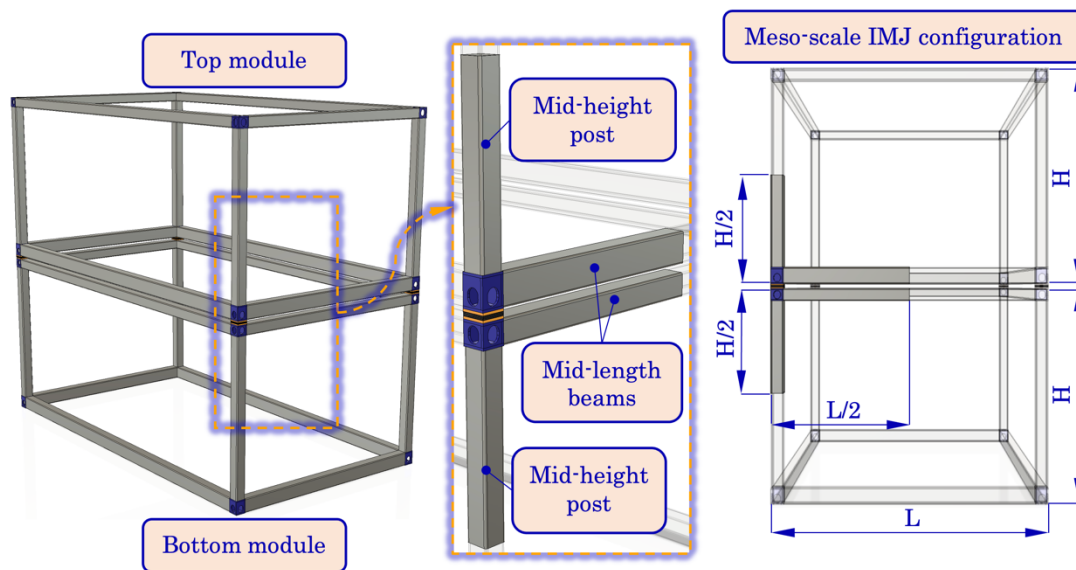


Fig. 2. Details of the meso-scale IMJ prototype.

Table 1. Test parameters.

Joint prototype	Bolting assembly	Beam-column joint
IMJ01	M20-27 SMA stud	Unstiffened
IMJ02	M20-27 SMA stud	Stiffened
IMJ03	M16-24 SMA stud	Unstiffened
IMJ04	M24, class 8.8 bolt	Unstiffened
IMJ05	M24, class 8.8 bolt	Stiffened
IMJ06	M27, class 8.8 bolt	Stiffened

3.2. Joint components and material properties

3.2.1. Beam-column sub-assemblages

Top and bottom beam-column sub-assemblages (Fig. 3) were made from standard cold-formed hollow members of S355J2H steel grade. The hollow sections have been joined to box corner fittings by complete joint penetration (CJP) groove welds, while cap plates were attached to each member's end through all around fillet welds. The role of the end-plates was to help realise the bolted connections between the samples and test frame. The box corner fittings (Fig. 4) were fabricated from 15-mm-thick steel plates of the same



S355H2H steel grade, joined together by CJP groove welding. Additionally, three of the tests included 100 mm x 100 mm x 10 mm triangular stiffener plates made of S355 steel, welded on each side of the beam-column joints.

The material properties of the steel frame parts were determined from standard tensile tests for metallic materials in accordance with the ISO 6892-1:2019 standard [29]. The uniaxial tensile tests were performed on proportional test pieces (coefficient of proportionality, $k = 5.65$) at room temperature using an Instron universal testing machine (Fig. 5). The testing rate was based on a strain rate, $\dot{\epsilon}_{Le}$, equal to 0.00025 s^{-1} which was kept constant throughout the entire test. The resulting mechanical properties (Table 2) were determined as the average of two test results for each frame part as shown in Fig. 6.

In general, the yield and tensile strength of all test pieces were greater than the nominal values recommended by Eurocode 3, Part 1-1 [30], while the slightly lower tensile strength of test piece B1 was attributed to the effect of residual stress as a result of cold-forming. The relatively large variation in material properties was explained by the fact that the coupons had been cut from the specimens post-test.

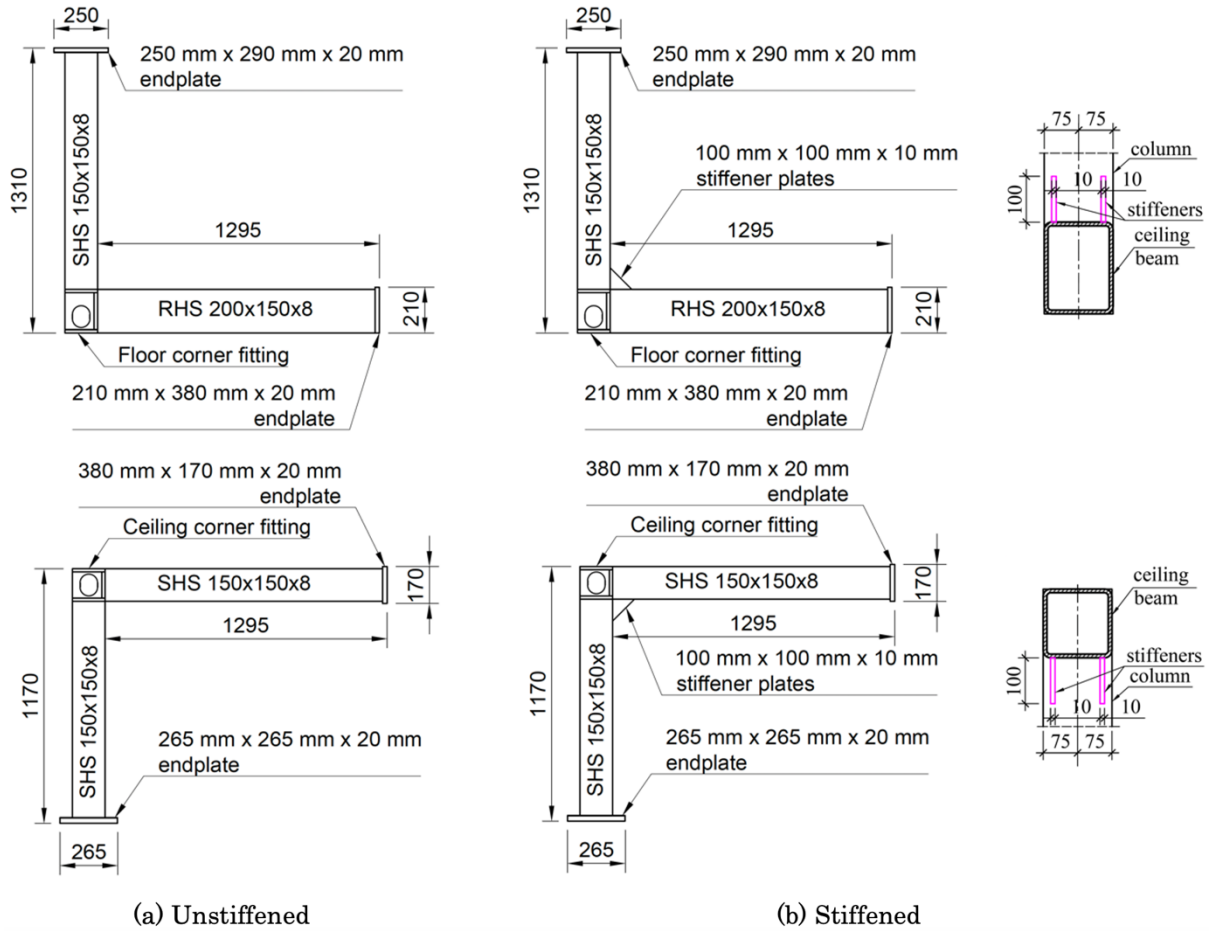


Fig. 3. Details of the steel beam-column sub-assemblages (units: millimetres).

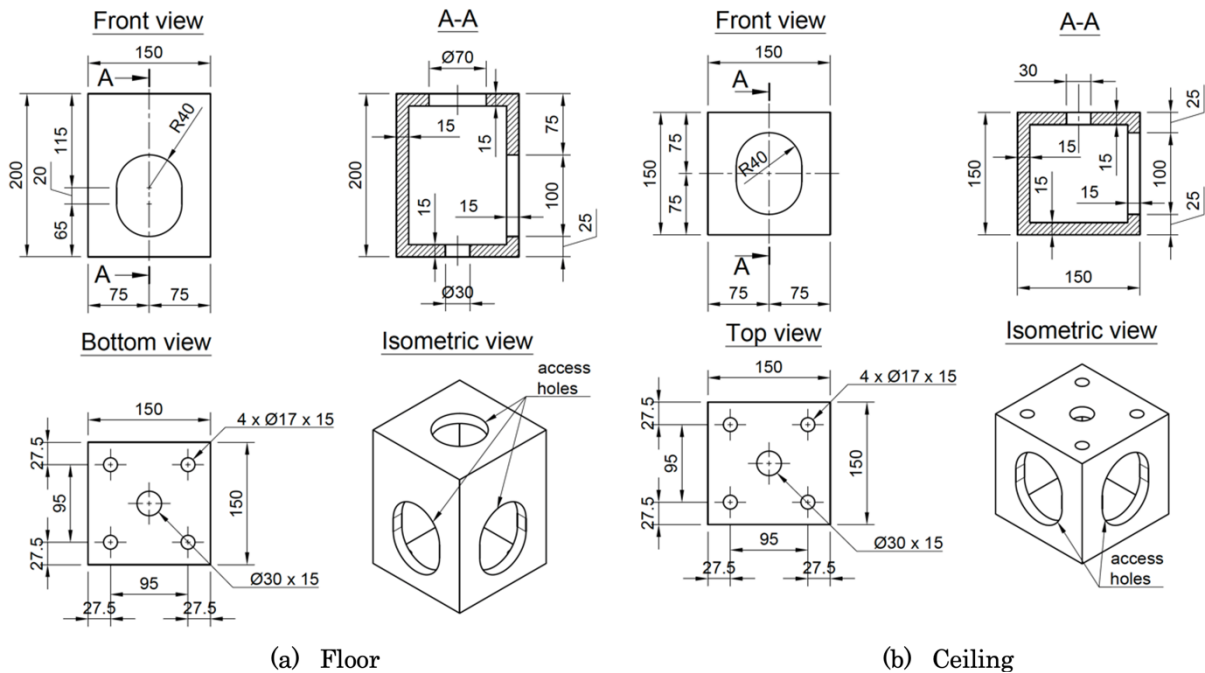


Fig. 4. Details of the box corner fittings (units: millimetres).

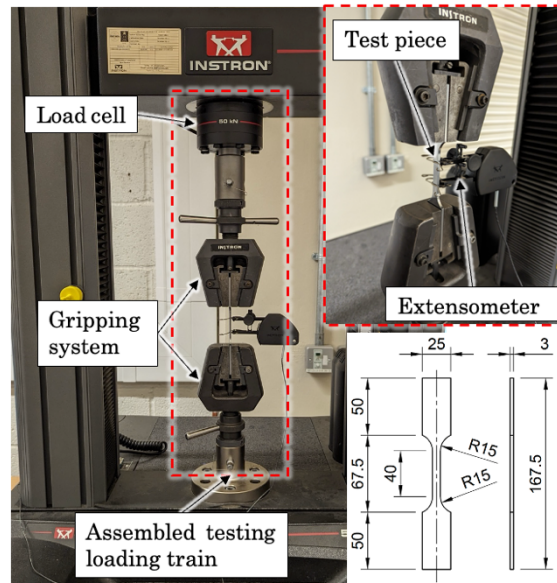


Fig. 5. Tensile test details (units: millimetres).

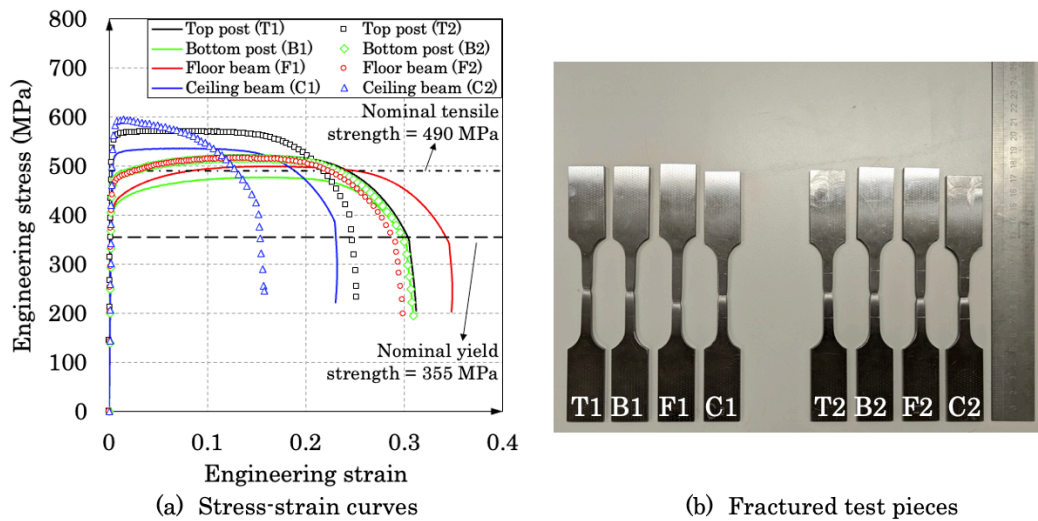


Fig. 6. Tensile test results.

Table 2. Material and section properties of the steel frame members.

Frame part	Section properties (mm x mm x mm)	Steel grade	E (GPa)	f_y (N/mm ²)	ϵ_y	f_u (N/mm ²)	ϵ_u	A (%)	W_{el} (cm ³)	W_{pl} (cm ³)
Top post	150 x 150 x 8	S355J2H	209	505	0.0044	546	0.1	28.2	188	226
Bottom post	150 x 150 x 8	S355J2H	205	438	0.0041	496	0.145	30.9	188	226
Floor beam	200 x 150 x 8	S355J2H	190	433	0.0043	507	0.149	32.4	283	344
Ceiling beam	150 x 150 x 8	S355J2H	202	541	0.0047	565	0.044	19.5	188	226

NOTE: (1) E is the modulus of elasticity, (2) f_y is the yield strength determined as the proof strength, $R_{p0.2}$, by the 0.2% strain offset method in lack of a flat yield plateau in any of the resulting stress-strain curves, (3) ϵ_y is the strain at yield strength, (4) f_u is the tensile strength, (5) ϵ_u is the strain at tensile strength, (6) A is the percentage elongation after fracture, (7) W_{el} is elastic section modulus, (8) W_{pl} is plastic section modulus.

3.2.2. Laminated elastomeric bearings

The laminated elastomeric bearings (LEBs) consist of two outer steel plates (150 mm x 150 mm x 15 mm), four high-damping rubber layers (150 mm x 150 mm x 4 mm) and three steel shims (150 mm x 150 mm x 3 mm), designed to achieve a shape factor of $S = 8.85$. A central hole (40 mm diameter) has been cut through the plates to accommodate the bolting assembly. The hole diameter was purposefully made larger than the hole diameter in the corner fittings to ensure that the bolt does not interfere with the inner surface of the bearing during the lateral cyclic loading imposed on the IMJ prototype. Blind holes (15 mm diameter x 10 mm deep) have been milled on the external face of the outer plates to insert the interlocking steel pins. The design details of the bearings are shown in Fig. 7. The material properties representative for the high-damping rubber (Table 3) were obtained from double-bonded shear tests based on data from the sixth loading cycle. A detailed account of the material characterisation tests for the HDR can be found in Corfar and Tsavdaridis [27].

The HDR bearing has been designed for the vertical load using equations (1)–(4) [31,28] to limit the total deflection of the rubber layers to less than 0.5 mm in order to avoid alignment issues during the specimen assembly, while still allowing sufficient shear flexibility for the purpose of the present connection design.

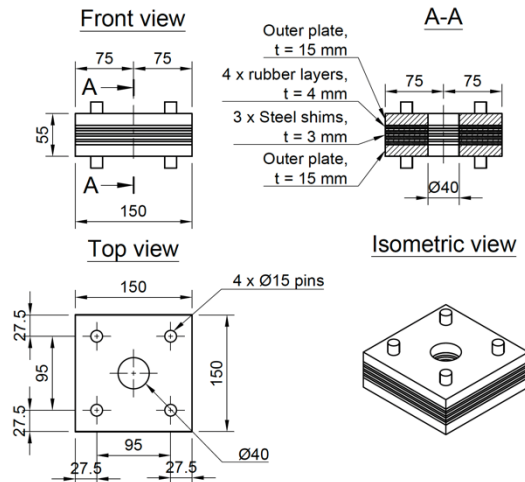


Fig. 7. Detailed drawings of the rubber bearings (units: millimetres).

$$S = (L^2 - \pi d^2/4)/4Lt \quad (1)$$

$$E_c = 5GS^2 \text{ (for } S > 3) \quad (2)$$

$$K_c = F/x \quad (3)$$

$$F = E_c A \quad (4)$$



Where S is the shape factor accounting for the central hole, L is the length of the rubber layer, d is the diameter of the central hole, t is the thickness of the rubber layer, E_c is the compression modulus, G is the shear modulus of rubber, K_c is the compressive stiffness, F is the compressive load, and A is the cross-sectional area of the bearing accounting for the central hole.

Table 3. Material properties of the high-damping rubber.

Property	Value
Hardness ^a	86 IRHD ^b
Shear modulus, G ^c	0.61 MPa
Effective damping ratio, ξ_{eff} . ^{b,c}	18.46 %

^a based on shear modulus at 5% shear strain

^b International rubber hardness degree

^c at 100% shear strain

3.2.3. Bolting assemblies

The bolting assemblies used in the tests included standard M24 x 150mm and M27 x 120mm full-thread hexagon head bolts (Fig. 8 (a) and (b)) made of class 8.8 high-strength steel (HSS) and double-end threaded superelastic shape-memory alloy (SMA) studs (Fig. 8 (c) and (d)).

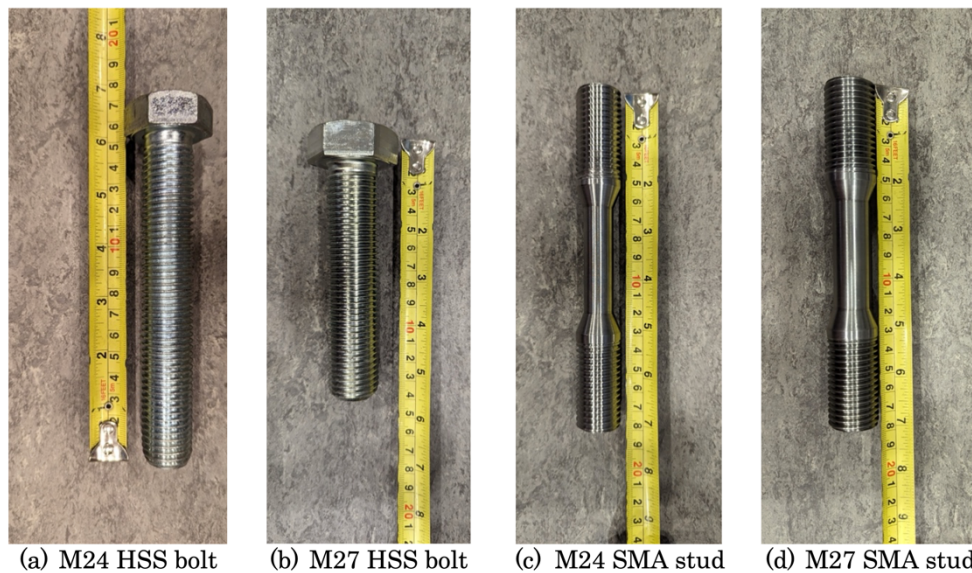


Fig. 8. Bolting assemblies.

The SMA studs (Fig. 9) have been machined from raw bars made of a Ni-rich (51 at.% Ni – 49 at.% Ti) NiTi alloy and then annealed at 500 °C for 30 min to adjust the final transformation temperatures (austenite finish temperature $A_f \approx 0^\circ\text{C}$) and provide the desired superelastic (SE) effect at ambient temperature. Based on recommendations from



previous tests [32,33], the NiTi SMA studs had a net threaded-to-shank diameter ratio of 1.25 to avoid premature fracture over the threaded area.

The results of the cyclic tensile tests for material characterisation of the NiTi alloy used in the SMA studs have been shown in Fig. 10 (a), indicating the first complete load-unload cycle up to a maximum deformation $\epsilon_{\max} = 4.50\%$, as well as the evolution of the stress-strain response of the material during fatigue cycling up to a maximum deformation $\epsilon_{\max} = 5.50\%$. The findings suggested satisfactory flag-shaped hysteresis associated with pronounced stress-induced phase transformation and good re-centring behaviour (recoverable strain $\epsilon_{\text{rec}} = 4.20\%$) during the first load-unload cycle. The repeated martensitic transformation reveals the phenomenon known as functional or transformation-induced fatigue (TIF) expressed by the accumulation of residual strain ($\epsilon_{\text{res}} = 1.83\%$), decrease in the transformation stress, and reduction of dissipated energy. The cyclic stabilisation (Fig. 10 (b)) of the NiTi sample was evident after 60 cycles, showing 3.70% recoverable deformation without residual strain accumulation, while strain ratchetting effects (also known as cyclic creep) characterised by shifting hysteretic loops along the strain axis were in good agreement with previous experimental findings [34,35].

The stress-strain curves in Fig. 10 are representative for 2 mm diameter dog-bone samples, yet the stress-strain response of the full-size SMA studs may vary to some extent due to size effects such as a ± 8 °C transformation temperature variation within the same material batch provided by the supplier. Nevertheless, the data obtained from the material test remains informative for predicting the behaviour of the SMA studs. The material properties for the superelastic SMA extracted from the first isothermal load-unload cycle shown in Fig. 10(a) were given in Table 4.

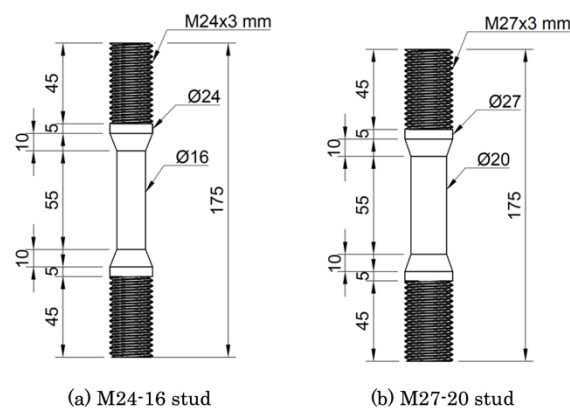


Fig. 9. Geometry of the double end threaded SMA studs (units: millimetres).

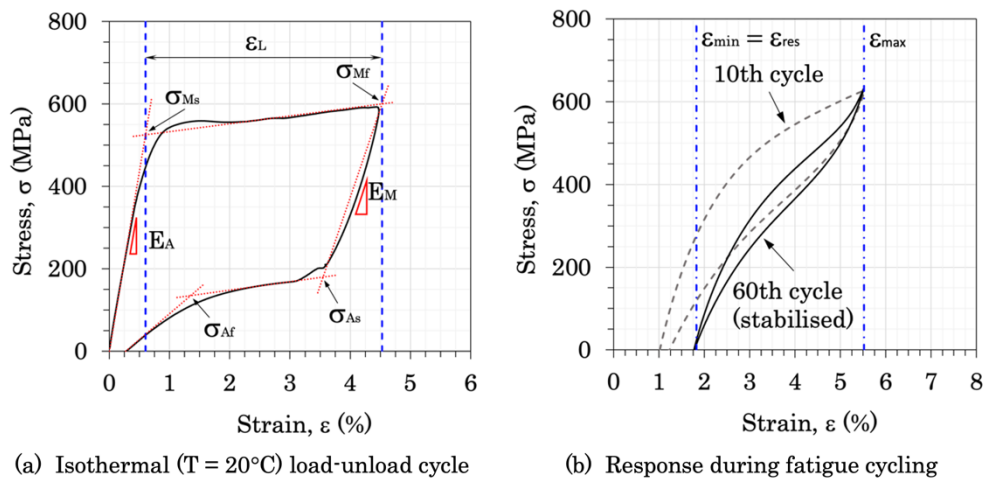


Fig. 10. Stress-strain behaviour of the NiTi alloy.

Table 4. Material properties of the superelastic NiTi alloy.

Property	Value
Young's modulus of austenite, E_A	88 GPa
Young's modulus of martensite, E_M	61 GPa
Forward transformation start stress, σ_{Ms}	525 MPa
Forward transformation finish stress, σ_{Mf}	600 MPa
Reverse transformation start stress, σ_{As}	180 MPa
Reverse transformation finish stress, σ_{Af}	135 MPa
Total transformation strain, ϵ_L	3.93 %

3.3. Test frame and instrumentation details

The loading system illustrated in Fig. 11 was designed to accommodate the loading on the test IMJ prototypes. The beam-column subassemblage with axial and in-plane lateral loading applied to the top column has been chosen for its ability to realistically replicate the deformed shape of unbraced modular frames subjected to a lateral load, including the contribution of the connecting framing members and the effect of the beam-column joint [36].

The constant, vertical axial load was applied at the top through the vertical jack, while a pair of horizontal actuators were used to exert the cyclic push and pull motion at the top of the prototype. The top and bottom end-plates of each specimen's column were bolted to the test (orange) rig frame using pinned supports to allow in-plane rotation. Hinge roller supports were attached at the ends of each beam to enable relative horizontal displacement between the top and bottom sub-assemblages.



Details of the potentiometer layout were shown in Fig. 12 (a). The in-plane lateral displacement applied at the top of the sample is recorded by the built-in linear variable displacement transformers of the servo-hydraulic actuators (T04) and is used to obtain the load-deflection hysteresis loops. Another two linear potentiometers (T01-02) have been arranged along the centrelines of the floor and ceiling beams to determine the relative horizontal displacement between upper and lower frames. A slide potentiometer (T03) was set up on the side of the floor and ceiling beams to monitor the vertical displacement near the rubber bearing. A total of 10 strain gauges were installed on the beam and posts near the beam-column joint zone as illustrated in Fig. 12 (b) to capture the strain distribution in key regions of the steel frame members.

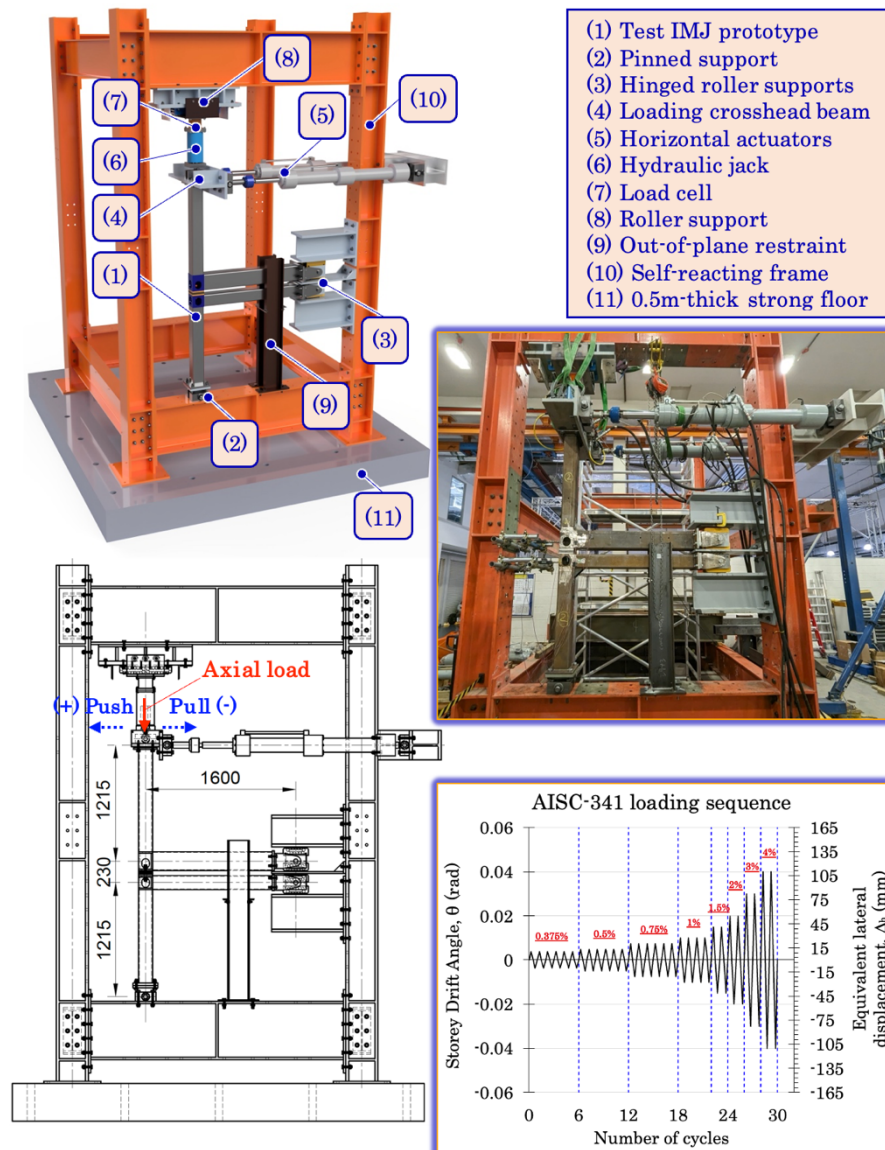


Fig. 11. Schematic representation of the test setup and loading system dimensions.

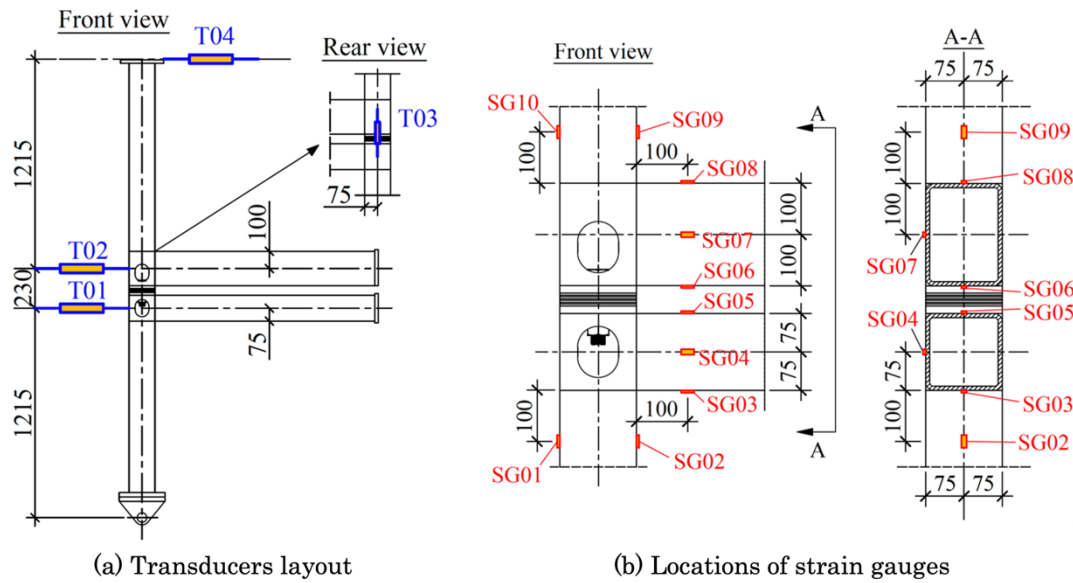


Fig. 12. Instrumentation details.

3.4. Load protocol

Based on a realistic on-site modular building installation sequence, a preliminary snug-tight condition was achieved in the hybrid IMC by the full effort of manually tightening the bolting assemblies using a spanner through the corner fitting access holes. The force-controlled compressive axial load of $N_{Ed} = 100$ kN was then applied at a rate of 1.67 kN/s to simulate the gravitational load imposed by upper building levels. The applied vertical load was equivalent to 5% of the compressive yield capacity of the column's cross-section, $N_{c,Rd}$, as defined in Eurocode 3, Part 1 [30] for members not susceptible to local buckling failure, and exerted a compressive stress of 4.7 MPa on the rubber bearing, which was maintained for 10 minutes before the commencement of the cyclic lateral load to account for the effect of creep in the rubber layers.

The axial load was then kept constant and vertical throughout all subsequent test stages, while the sample was subjected to the displacement-controlled standard FEMA/SAC loading sequence [37], following the prequalification and cyclic qualification testing provisions as per ANSI/AISC 341-22 [38]. The equivalent lateral displacement (Where θ is the inter-storey drift angle (also known as chord rotation), $\Delta\eta$ is the equivalent lateral displacement applied at the top of the column, and H_{storey} is the total height of the specimen (2,750 mm).

Table 5) applied at the top of the column, Δ_h , has been determined using equation (5). The horizontal drift ratio was applied in a quasi-static manner at a rate of 10mm/min to limit the influence of dynamic effects such as those arising from the inertial forces of the joint



assemblies. The maximum lateral drift level that could be achieved at the top of the specimen was that of $\theta = \pm 0.04$ rad because of constructional limitations related to the test frame and loading system.

$$\theta = \Delta_h / H_{\text{storey}} \quad (5)$$

Where θ is the inter-storey drift angle (also known as chord rotation), Δ_h is the equivalent lateral displacement applied at the top of the column, and H_{storey} is the total height of the specimen (2,750 mm).

Table 5. Cyclic loading sequence.

Load step	Inter-storey drift angle, θ	Equivalent lateral displacement, Δ_h	Number of cycles
1	0.00375 rad	10.3 mm	6
2	0.005 rad	13.8 mm	6
3	0.0075 rad	20.6 mm	6
4	0.01 rad	27.5 mm	4
5	0.015 rad	41.3 mm	2
6	0.02 rad	55 mm	2
7	0.03 rad	82.5 mm	2
8	0.04 rad	110 mm	2

The following potential failure modes have been envisaged for the test IMJ prototypes:

- Fracture due to shear failure in the threaded regions of the SMA studs
- Bolt shank fracture under combined bending and shear deformation
- Rubber layer fracture under repeated large shear strain cycles
- Rubber layer delamination (signalling poor fabrication quality)
- Weld cracking and failure at the beam-column connection
- Inelastic failure (plastic hinge developed) in the beams and/or posts members near the beam-column joint zone (least likely due to the design of the hybrid IMC)

4. Test results and discussion

4.1. General behaviour

The main test observations for the hybrid inter-module joints and the connection components during the cyclic tests were shown in Fig. 14, while a summary of the failure modes and other test phenomena was given in

Table 6.



At the end of the 10-minute creep stage, it was reasonably assumed that the bolting assemblies experienced a partial loss of pre-tension due to the deflection of the rubber layers, losing the preliminary snug-tight condition. While this effect led to slightly lower shear stiffness in the connections during the early cycles, it allowed for a larger deformation capacity and provided a strength reserve by effectively delaying the full contribution of the studs and bolts to the force-transfer mechanism of the connections.

The following observations were common between all test specimens. At the onset of cyclic loading, the inter-storey drift occurred mostly in the inter-module connection (up to the end of the $\pm 0.5\%$ drift ratio cycles), as expected due to the low shear stiffness of the rubber layers, highlighting the rubber bearing as the major contributor to the joint's response to small-amplitude lateral loading cycles (Fig. 13 (a)). During these initial stages, it was observed that the bolting assemblies were allowed to translate horizontally together with the upper box corner fittings until the gap provided by the bolt hole tolerance was fully closed and the bolting assemblies became locked in a bending deformation state (Fig. 13 (b)). Then, as the loading sequence progressed towards the larger drift ratio levels, the shear deformation of the rubber layers increased up to the point when the contribution of the flexural stiffness of the beam-column sub-assemblages was evident as shown by the pronounced deflection of their framing members (Fig. 13 (c) and Fig. 14 (a)). The ceiling beam suffered a more noticeable deflection than the floor beam, explained by the smaller size of its cross-section.

Taking a closer look at the connection level, the rubber bearing was subjected to the combined effect of axial load and horizontal shear throughout the cyclic loading protocol. Due to the quasi-static nature of the tests and the low thickness of the rubber layers, heat build-up was not expected to be an issue, which was confirmed with the aid of a thermal camera, registering a constant temperature throughout the first test. There was no gap opening between the box corner fitting end-plates and the outer plates of the rubber bearing, while the top and bottom surfaces remained reasonably parallel even at maximum shear deformation levels, as shown in Fig. 14 (b). This was partly due to the constant axial load acting vertically on the corner post all throughout the test and due to the shear and flexural flexibility of the rubber bearing which accommodated the rotational deformations imposed preventing any uplift. While the tolerance in the interlocking pin holes was limited to 1 mm – 2 mm, no relative sliding was noticed between the steel plate surfaces during the repeated load reversals, suggesting that the four pins on the rubber bearing outer plates were quickly engaged in the horizontal shear, transferring the force



to the rubber bearing and perhaps with some contribution from the friction resistance. For the present tests, the contact surfaces of the box corner fittings were cleaned by wire-brushing, with loose rust removed as per Eurocode 3, Part 1-8 [39] and EN 1090, Part 2 [40], while the contact surfaces of the rubber bearing outer plates were as resulted from the milling process.

As the rubber bearings for the hybrid IMC were smaller than typical bridge bearings or seismic isolators, the dimensional tolerances were also tighter, requiring special attention to quality control. The finish quality on the steel contact surfaces should also be given due consideration, to ensure good friction resistance and avoid relative slipping between connection components.

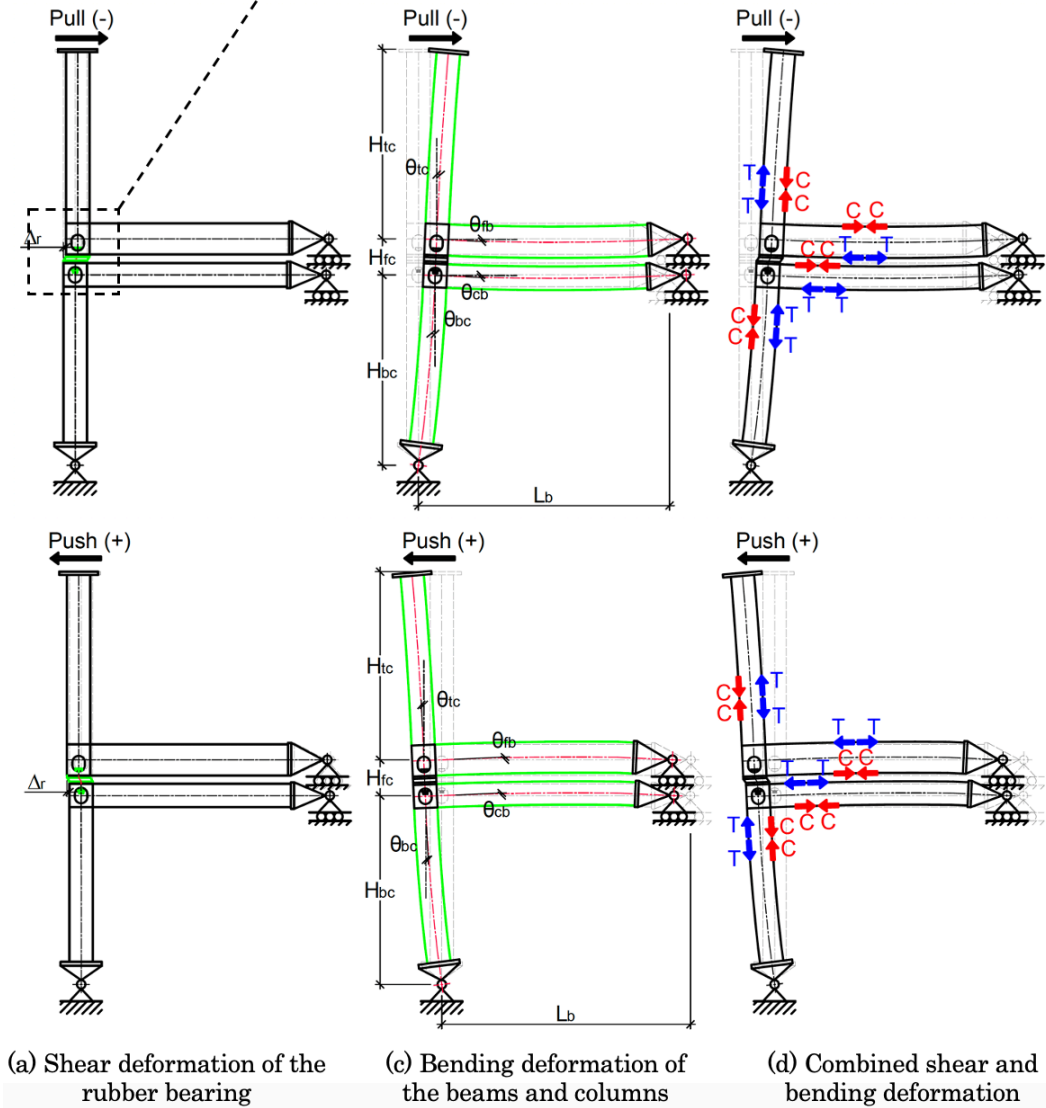
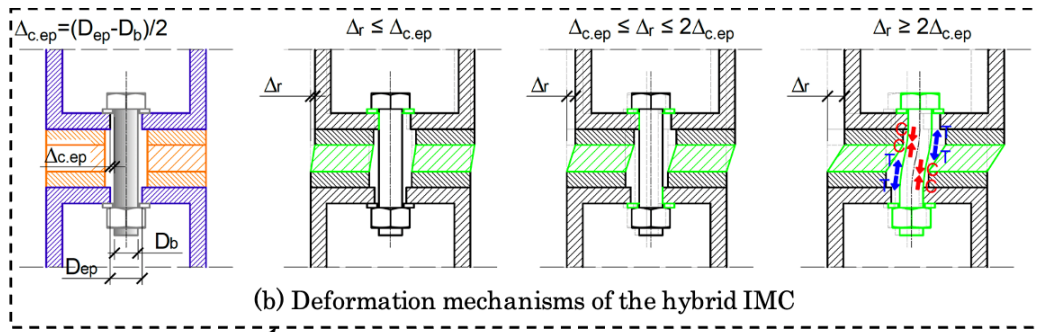


Fig. 13. Deformation mechanisms of the hybrid IMJ.

4.2. Test phenomena and controlling failure modes

To identify the differences between the tests as well as the effect of the test parameters considered, each specimen was discussed separately.



The test on prototype IMJ01 included an M27-20 SMA stud and unstiffened beam-column connection. Half-nuts were also added to determine if using two nuts would have any meaningful effect in preventing self-loosening in this particular case. After completing 26 cycles without signs of damage to the naked eye, a loud sound announced the sudden fracture of the SMA stud during the reversal loading of the first $\pm 3\%$ drift ratio cycle at a lateral load of 52 kN, and the test was stopped.

During the test on specimen IMJ02 with the same size of SMA stud and stiffened beam-column connection, the first $\pm 3\%$ drift ratio cycle was completed, while the SMA stud was fractured during the 28th cycle at a similar lateral load as IMJ01 (49 kN). This result revealed a favourable effect of the intra-module connection stiffeners over the load-transfer mechanism of the inter-module connection as the SMA stud survived one extra loading cycle before being loaded beyond its ultimate capacity. Moreover, the comparable failure load levels proved the consistency of the test results and confirmed the limited influence of the lock nuts as the SMA studs were likely already loosened by the deflection of the rubber bearing.

The last of the SMA specimens was IMJ03, which included an M24-16 SMA stud and stiffened beam-column connections. During this test, the specimen completed 25 cycles, while the smaller SMA stud failed during second $\pm 2\%$ drift ratio cycle, confirming the key role of the bolting assembly in the lateral response of the joint at this drift ratio level, as well as the predictability of the results as the smaller size SMA stud performed worse in terms of lateral load capacity.

During the test on specimen IMJ04, the M24 HSS bolt experienced significant bending deformation as well as damage to the threads. The onset of weld cracking at the ceiling beam-column connection (Fig. 14 (c)) was noticed after the peak was reached in the positive loading direction during the second $\pm 4\%$ drift ratio cycle, causing the peak lateral load in the reverse direction to fall to 85% of the previous maximum. At the end of the load programme, the reduction was still well above the 20% failure criterium defined in the FEMA/SAC guidance [37], yet the controlling failure mode could be identified as the weakened beam-column connection. This finding was in good agreement with results from similar tests [41–43], emphasising once more the importance of the weld quality at these highly stressed regions.

Specimen IMJ05 suffered similar damage levels to the HSS bolt, while the test was completed without any damage to the beam-column connection due to the effect of the



stiffener plates. In the positive loading direction of the $\pm 4\%$ drift ratio cycles, a malfunction of the control system caused the two actuators to enter load reversal before reaching the peak lateral displacement corresponding to 4% drift ratio. Nevertheless, the results from specimen IMJ04 and IMJ06 provided sufficient evidence to suggest that the lateral load capacity corresponding to the 4% drift ratio would have been very close to 66 kN, supporting the validity of the present result.

The last of the HSS specimens was IMJ06, which completed the full 30 cycles of the FEMA/SAC protocol without any damage to the beam-column connections or framing members, while the deformation of the bolting assembly was less pronounced due to its larger diameter.

An overview of the failure modes of the bolting assemblies was shown in Fig. 14 (d). While the ultimate tensile strength of the Ni-Ti alloy in the SMA studs was exceeded at different drift ratio levels, the type of failure mode was identical for all samples, as revealed by the similar fracture patterns which occurred in the top of the stud, at the border between the reduced diameter and the transition zone to the threaded ends. The direction of the fracture development was revealed by a small wedge present in the M27-20 SMA stud samples that broke off from the highly stressed region on the right hand side, showing that two cracks were initiated in the tension zone and were eventually joined on the compression zone on the left hand side. This finding was in good agreement with the results reported by the proof-of-concept FEA study [27], which highlighted the same highly stressed wedge at the base of the transition zone of the SMA stud. The same type of deformation was also evident in the shanks of the HSS bolts, suggesting that the yield strength was exceeded, while the ultimate strength of the 8.8 class bolts was not, as no fracture occurred in the threads.

Although the SMA bolts failed before the full protocol was completed, the location of the fractures proved that the dog-bone shape design of the SMA studs was effective in shifting the damage away from the threads which were known as vulnerable zones prone to premature fracture. The net threaded-to-shank diameter ratios of the M27-20 and the M24-16 SMA studs were 1.25 and 1.375 respectively. Overall, these consistent, repetitive failure modes highlighted the limited randomness and supported the validity of the test results.



4.3. Demountability and reuse potential

To showcase the demountability of the hybrid inter-module connection, it is worth noting the ease of disassembling the joint prototypes to change specimens between tests. In spite of the deformed shapes of the HSS bolts, none were jammed, allowing for easy unfastening using a regular spanner.

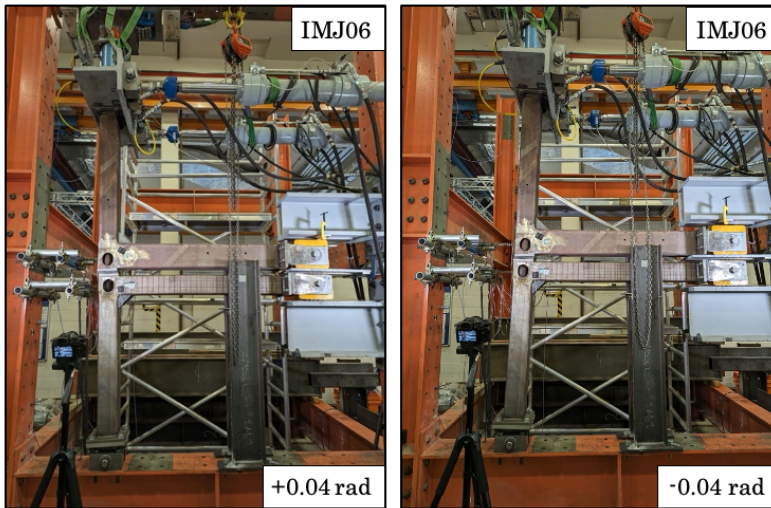
At the end of the tests on specimens IMJ04, IMJ05, and IMJ06, the rubber bearings were removed from the joint assembly for inspection. As shown in Fig. 14 (e), the bearings displayed various levels of permanent deformation caused by the permanent set of the rubber. Since most of the set in rubber occurs on the first few loading cycles, it may be concluded that the repeated tests on the bearings from specimens IMJ04 and IMJ06 did not have a significant cumulative effect and did not have a negative impact on subsequent retesting. Out of the three bearings, the most prominent deformation was observed in the rubber bearing from IMJ04. The comparison with specimen IMJ05 suggested that the stiffened beam-column connection had a more significant part in the force transfer mechanism, reducing the deformation demand in the bearing. When comparing specimens IMJ05 and IMJ06, the permanent deformation was less evident, while the slightly larger deformation in specimen IMJ05 was explained by the smaller diameter of the M24 bolt which influenced the horizontal stiffness of the IMC, causing larger deformation in the rubber layers.

Despite the noticeable permanent deformation, the bonds between the rubber layers and reinforcing steel plates were still in perfect condition with no signs of delamination in either one of the three rubber bearings owing to the high-quality of their fabrication. This observation is particularly relevant, given the higher manufacturing costs of the rubber bearings compared to the other connection components. Overall, these findings offered valuable insights into the resilience and reuse potential of the rubber bearing component. The favourable behaviour of the bearings that underwent repeated cyclic loading protocols (representative of aftershocks) was reflected by their condition at the end of the tests which was deemed satisfactorily to be reused.

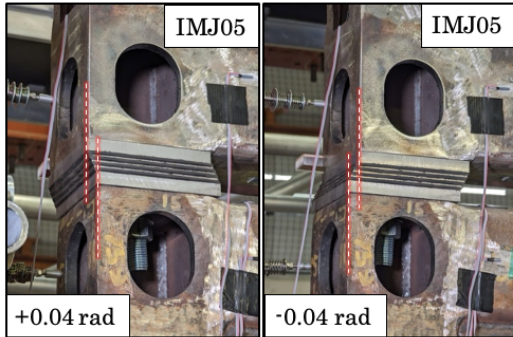


Table 6. Summary of test phenomena and controlling failure modes.

Specimen	Observed behaviour
IMJ01	SMA stud fracture, Test stopped during the reverse loading of the first cycle of $\pm 3\%$ drift ratio
IMJ02	SMA stud fracture, Test stopped during the reverse loading of the second cycle of $\pm 3\%$ drift ratio
IMJ03	SMA stud fracture, Test stopped during the reverse loading of the second cycle of $\pm 2\%$ drift ratio
IMJ04	HSS bolt bending, Weld cracking at bottom beam-column joint, Last cycle completed with reduced strength and stiffness
IMJ05	HSS bolt bending, No signs of damage at intra-module connections, Last cycle completed without signs of reduced capacity
IMJ06	HSS bolt bending, No signs of damage at intra-module connections, Last cycle completed without signs of reduced capacity



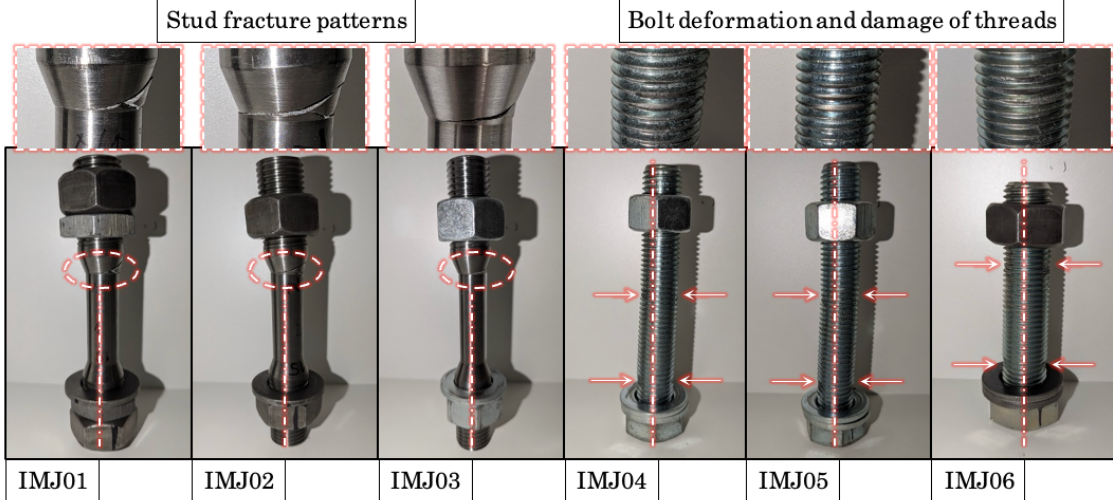
(a) Deflection of beam-column sub-assemblages at peak inter-storey drift angles



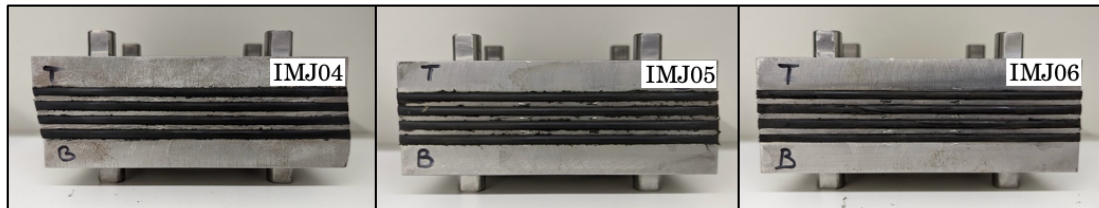
(b) Shear deformation of the rubber layers



(c) Weld crack at beam-column connection



(d) State of the SMA studs and HSS bolts at the end of the tests



(e) Permanent deformation of the rubber bearings

Fig. 14. Test observations of IMJs and connection components during cyclic loading.



4.4. Hysteretic behaviour

The relationship between the applied lateral displacement and the corresponding reaction force at the top of the IMJ prototype generated the hysteresis loops shown in Fig. 15, offering insights into the seismic response of the hybrid joints. A summary of the main lateral load capacities and secant stiffnesses of the test specimens was given in Table 7.

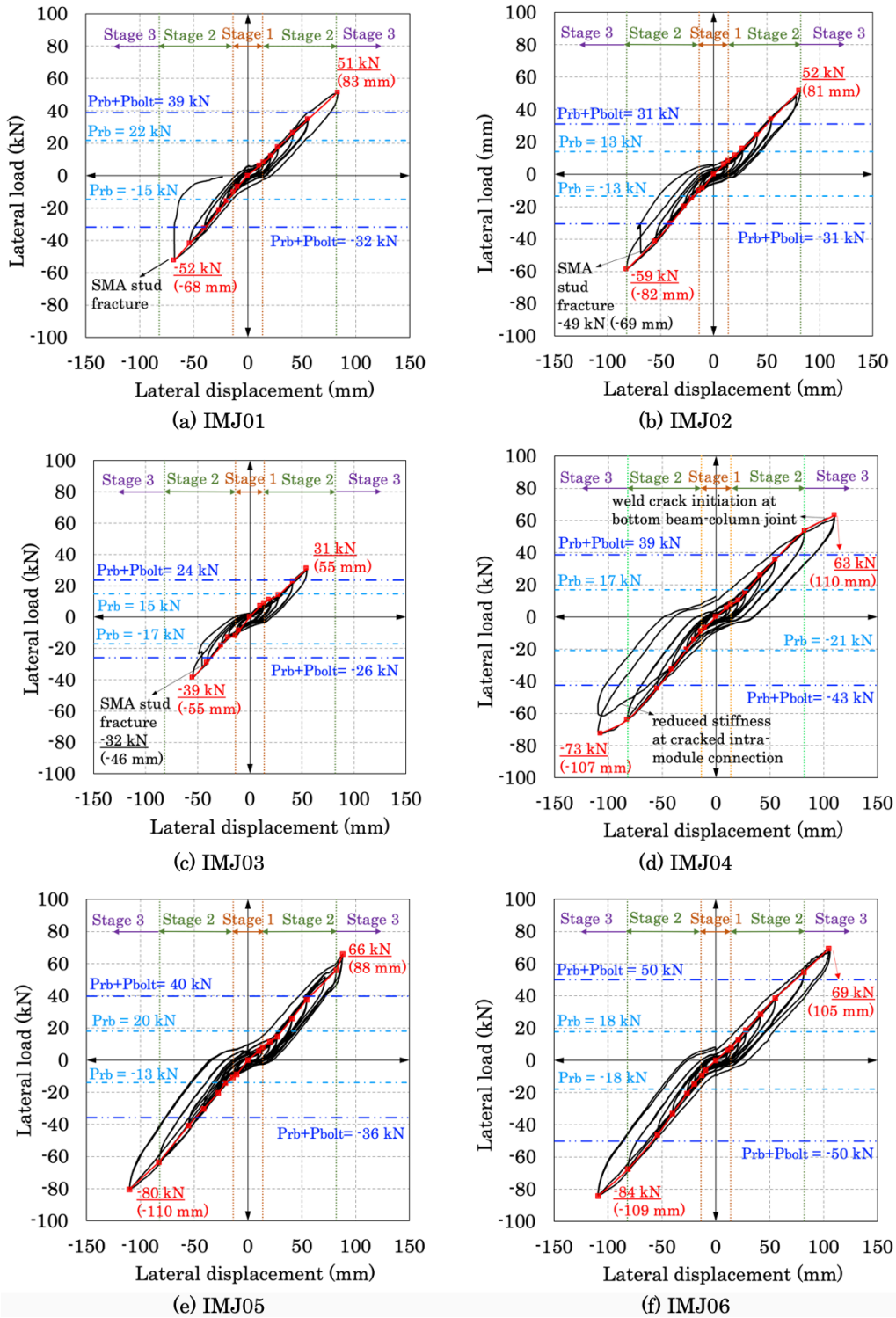


Fig. 15. Hysteretic curves.

All six specimens displayed similar reversed S-shaped curves with well-defined, stable hysteresis and multiple stages indicating the successive activation of different connection components.



During the first stage (0 to $\pm 0.5\%$ drift ratio), the rubber bearing was immediately engaged by the horizontal shear developed between the box corner fittings of the IMC due to the frictional resistance of the steel contact surfaces. On closer inspection, the major contribution of the rubber bearing was further highlighted by the low strength and pronounced nonlinearity of the curves, described by high initial stiffness followed by quick softening leading to increasing stiffness at higher strains, typical of filled rubber under shear loading. The curves also exhibited the stress-softening effect (or Mullins' effect [44]) typical for rubber under repeated shear straining.

In the second stage ($\pm 0.5\%$ to $\pm 3\%$), the bolting assembly was completely engaged in a bending deformation as the bolt hole clearances closed under the relative horizontal displacement of the box corner fittings. This limited the shear deformation in the rubber layers, initiating the partial involvement of the framing members through their flexural stiffness. The failure of the SMA studs confirmed their critical role in the force transfer mechanism of the connection during this stage, while the behaviour recorded after the failure offered valuable insights into the redundancy of the hybrid joints. As shown by specimens IMJ02-03, the moment of failure was marked by a sudden drop in the lateral load capacity, which was now provided only by the rubber bearing and framing elements, as the path was resumed with reduced stiffness. It may also be assumed that the interlocking steel pins on the rubber bearings' outer plates played an important part as they acted as shear keys and stoppers for the rubber bearing, allowing the joints to develop the necessary strength reserve.

The third and final stage ($\pm 3\%$ and beyond) was identified by the comparison between the stiffened and unstiffened beam-column connections, signalling the prominent influence of the intra-module connection in the force resisting mechanism developed at high drift ratios. Secondly, the size of the bolting assembly was also a differentiator in the joint's behaviour in the third stage, as would be expected by the increased deformation suffered by the bolt. Overall, the IMJs displayed stiffer behaviour in the negative loading direction (pulling direction for the actuators), which was attributed to the lack of symmetry of the one-sided T-shaped specimens, with rigid intra-module beam-column connections only on one side of the assemblage. This finding was in good agreement with the results from other experimental work that employed one-sided T-shaped joints with column loading [41,43].



The shear deformation demand of the rubber bearings at different drift ratios (Fig. 16) was estimated as the relative horizontal displacement, Δ_r , determined by the difference between the measurements from transducers T02 and T01. The corresponding shear strain percent, γ , was then determined as the ratio between the shear displacement and the total thickness of the rubber. Based on these results, the equivalent lateral load developed in the bearings at maximum drift ratio, P_{rb} , was added to the plots in Fig. 15 to illustrate the contribution of the rubber bearings to the lateral load capacity of the hybrid IMJs. P_{rb} was obtained by equation (6), where $G_{i\%}$ was the shear modulus of the rubber corresponding to $i\%$ shear strain (also given in Fig. 16) and A was the cross-sectional area accounting for the central hole.

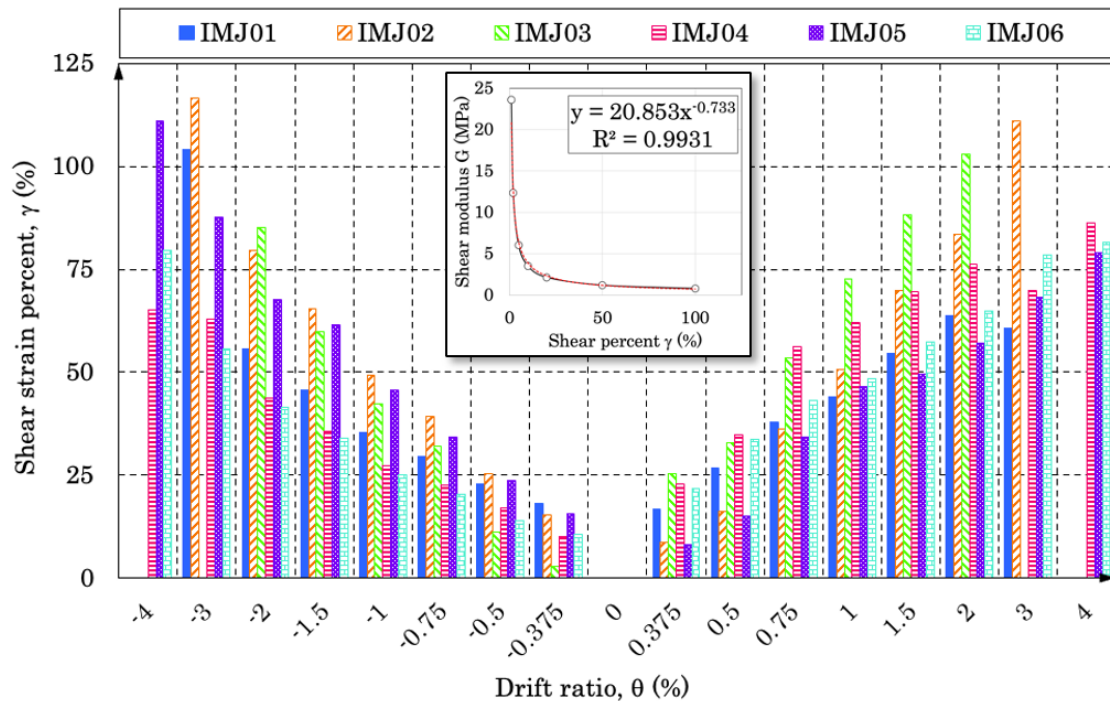


Fig. 16. Shear deformation demand in the rubber bearings.

Moreover, the equivalent lateral load developed by the bolts, P_{bolt} , was added to the plots in Fig. 15 to reflect the combined capacity of the rubber bearing and bolting assembly in relation with the total lateral load capacity of the joint assemblies. The results showed that the maximum lateral load capacities of the HSS bolt specimens and corresponding failure loads of the SMA stud specimens were actually higher than the design predictions, confirming the multi-stage hybrid mechanical behaviour of the IMC in which the bolting assemblies were not fully engaged from the beginning of the loading cycle. The test lateral load capacities exceeded the predicted resistances by 19% to 95%, suggesting that it would be overconservative to design the hybrid IMJs based only on the combined contribution of



the rubber bearing and bolting assembly, ignoring the additional contribution from the steel frame members.

The combined and individual contributions of the joint components to the lateral load capacity of the IMJs were further highlighted in Fig. 17, where P_{test} was the lateral load capacity at maximum drift ratio reached during the test in each direction. The results showed that the ratio of the combined response of the rubber bearing and bolting assembly to the total lateral load capacity of the joints varied between 0.6 and 0.76 in the positive loading direction and between 0.45 and 0.66 in the negative loading direction, showcasing a significant contribution of the hybrid IMC to the lateral load capacity at joint level. The negative loading direction exhibited a larger influence from the steel frame (up to 55% in IMJ05), which can be correlated with the overall higher lateral load capacity and stiffness recorded in this direction. The larger contribution of the rubber bearing in IMJ03 was correlated to the larger deformation demand observed in Fig. 16, explained by the reduced stiffness of the M24-16 SMA stud causing more force to be transferred to the rubber bearing.

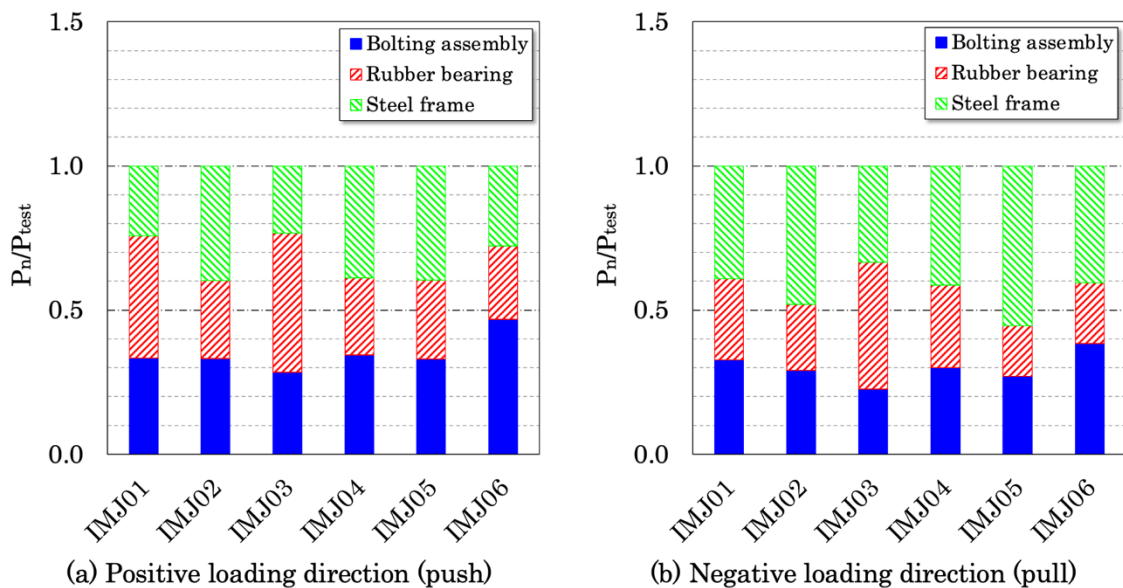


Fig. 17. Lateral load contribution ratios of the hybrid IMJ components.

P_{bolt} was estimated by equations (7) and (8) as the shear force corresponding to the bending resistance of the bolt rod (see also Fig. 25). Since the HSS bolts exhibited plastic deformation at the end of the tests, it was considered sensible to use the yield strength, f_{yb} , when calculating the bending resistances, $M_{Rd,bolt}$. However, in the case of the SMA studs which were all fractured, the forward transformation finish stress, σ_{MF} , was used instead, in lack of data about the ultimate tensile strength of the Ni-Ti alloy from the



material characterisation tests. The section modulus, $W_{el.bolt}$, of the HSS bolts was determined based on the tensile diameter in the threaded region, while for the SMA studs, the reduced diameter between the transition zones was adopted instead.

$$P_{rb} = G_{i\%}A \quad (6)$$

$$P_{bolt} = 2M_{Rd.bolt}/h_{rb} \quad (7)$$

$$M_{Rd.bolt} = f_{yb}W_{el.bolt} \quad (8)$$

Where P_{rb} is the lateral load developed in the rubber bearings, $G_{i\%}$ is the shear modulus of rubber corresponding to $i\%$ shear strain, A is the cross-sectional plan area of the rubber bearing accounting for the hole, P_{bolt} is the shear force corresponding to the bending resistance of the bolt rod, $M_{Rd.bolt}$ is the bending resistance of the bolt rod, h_{rb} is the height of the rubber bearing, f_{yb} is the yield strength, and $W_{el.bolt}$ is section modulus of the bolt rod.

Table 7. Summary of lateral load capacity and secant stiffness of hybrid IMJs.

Specimen	Loading direction	$P_{0.5\%}$ (kN)	$K_{0.5\%}$ (kN/mm)	$P_{2\%}$ (kN)	$K_{2\%}$ (kN/mm)	P_{max} (kN)	K_{max} (kN/mm)	Last cycle reached
IMJ01	(+)	8.2	0.56	34.7	0.62	51.4	0.62	1 st cycle at 0.03 rad
	(-)	-10.4	0.81	-42.0	0.78	-52.3	0.77	
IMJ02	(+)	8.1	0.60	33.9	0.62	51.7	0.64	2 nd cycle at 0.03 rad
	(-)	-10.2	0.75	-41.4	0.75	-58.9	0.72	
IMJ03	(+)	8.8	0.64	30.8	0.56	= $P_{2\%}$	= $K_{2\%}$	2 nd cycle at 0.02 rad
	(-)	-12.1	0.88	-38.8	0.71	= $P_{2\%}$	= $K_{2\%}$	
IMJ04	(+)	7.6	0.56	35.6	0.65	63.1	0.57	2 nd cycle at 0.04 rad
	(-)	-9.2	0.66	-44.4	0.81	-72.5	0.68	
IMJ05	(+)	8.0	0.59	37.4	0.69	65.8	0.75	2 nd cycle at 0.04 rad
	(-)	-10.7	0.77	-40.8	0.74	-80.3	0.73	
IMJ06	(+)	8.2	0.57	38.6	0.70	69.2	0.66	2 nd cycle at 0.04 rad
	(-)	-9.3	0.71	-46.3	0.85	-84.3	0.77	

NOTE: $P_{0.5\%}$ and $K_{0.5\%}$ are the lateral load capacity and corresponding secant stiffness at 0.5% drift ratio, $P_{2\%}$ and $K_{2\%}$ are the lateral load capacity and corresponding secant stiffness at 2% drift ratio, P_{max} and K_{max} are the maximum lateral load capacity and corresponding secant stiffness reached during the test. Values correspond to the first cycle of each loading amplitude.

4.5. Skeleton curves

The skeleton (or envelope) curves shown in Fig. 18 were obtained from the peak strength reached during the first cycle at each drift ratio. The bolt size and intra-module connection stiffness had a limited effect on the lateral load capacity of the specimens up to $\pm 0.5\%$ drift ratio (± 13.8 mm lateral displacement). In the latter stages of deformation, specimens IMJ05 and IMJ06 stood out with higher lateral load capacities than specimen IMJ04, due to the addition of stiffeners at the intra-module connection, while the slightly higher overall capacity of IMJ06 was attributed to the additional impact provided by the bolting assembly with a larger diameter.

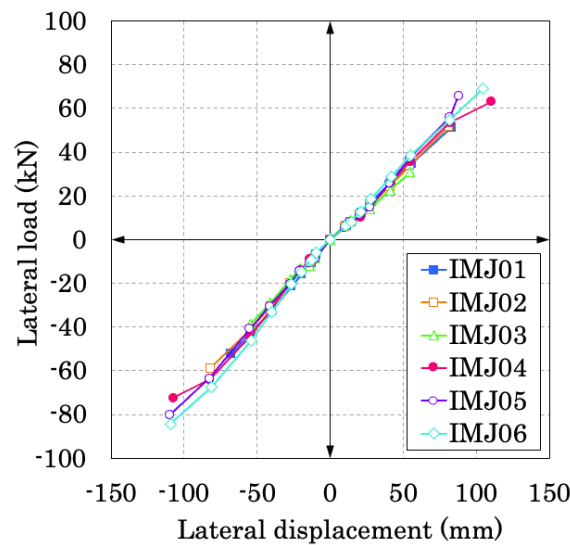


Fig. 18. Skeleton curves.

4.6. Joint classification

Fig. 19 illustrated the stiffness and strength classification of the ceiling and floor beam-column connections according to the boundaries defined by Eurocode 3, Part 1-8 [39]. Both the ceiling and floor beam-column connection were classified as semi-rigid, partial-strength. From the perspective of strength characteristics, neither the floor nor the ceiling beams were able to develop their full strength, owing to shear flexibility of the rubber bearing which combined with bending of the bolting assemblies, influenced the limit state of the hybrid IMJs, reducing the forces transferred to the beams as previously shown in Fig. 17. From the point of view of stiffness, both joints were conservatively classified as semi-rigid, indicating that the nonlinear behaviour of the beam-column connections should be explicitly considered in the macro-mechanical models for global analysis. However, in the design of steel modular buildings, it is recommended that the intra-module connections are designed as rigid, to ensure the volumetric units perform elastically. It must be noted that the stiffness classification was based on theoretical formulae for the rotation angles which did not account for the presence of stiffeners at the beam-column joints, hence the present classification remains conservative.

The bending moments in the ceiling and floor beams, namely M_{cb} and M_{fb} , were obtained from equations (19) and (20) while the corresponding rotation angles, θ_{cb} and θ_{fb} , were calculated using equations (21) and (22) as shown in Fig. 25. The classification boundaries were based on the plastic moment resistance of the beams, $M_{b,pl,Rd}$, calculated by equation (9) using the section and material properties given in Table 2.

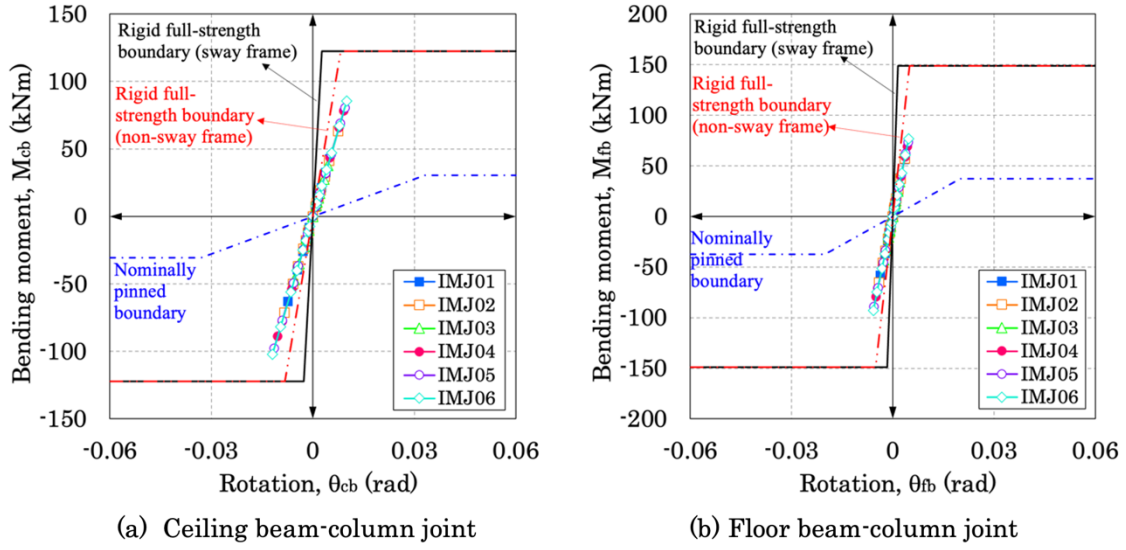


Fig. 19. Classification of beam-column joints based on moment-rotation envelope curves.

$$M_{b,pl,Rd} = W_{pl} \times f_y \quad (9)$$

Where $M_{b,pl,Rd}$ is the plastic moment resistance of the beams, W_{pl} is the plastic section modulus, and f_y is the yield strength.

4.7. Stiffness degradation

Fig. 20 indicates the variation of the stiffness characteristics of the joints with the progression of cyclic loading, represented by the secant stiffness, K_i , and the stiffness degradation factor, ζ_i , obtained by equations (10) and (11) respectively. The overall stiffer response of the joints in the negative (pulling) loading direction was confirmed in Fig. 20 (a), while the most rapid stiffness changes were observed during the small amplitude cycles in both loading directions. These changes were attributed to the stress-softening of the high-damping rubber and the partially loose state of the bolting assemblies, which experienced various movements during these early stages due to the different bolt hole clearances. After the 1% drift ratio level, the overall stiffness of the connections increased steadily, owing to the increasing contribution of the frame members as all bolting assemblies were engaged completely by the shear deformation of the bearings at this stage, peaking during the 2% drift ratio cycle. Fig. 20 (b) demonstrated the remarkable performance of the samples, which generally showed limited degradation rates in both loading directions, emphasising the effectiveness of the hybrid IMC in hindering the cumulative damage in the joints. Overall, specimen IMJ06 outperformed the others finishing the test with about 20% stiffness increase, showcasing the favourable influence of the M27 HSS bolt and stiffened intra-module connections.

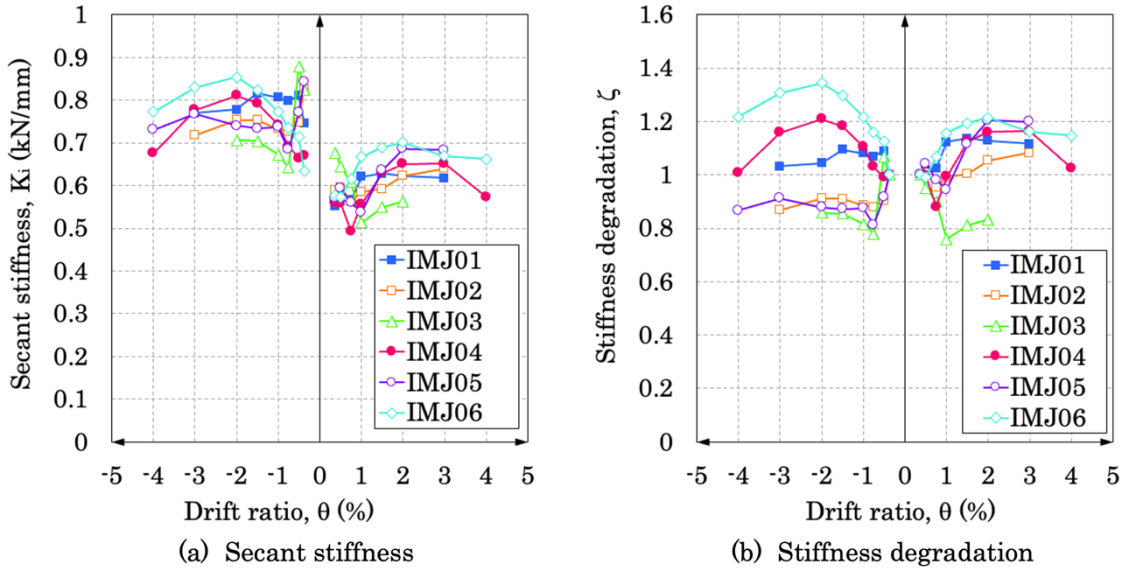


Fig. 20. Stiffness characteristics of hybrid IMJs.

$$K_i = \frac{P_{i,max}}{d_{i,max}} \quad (10)$$

$$\zeta_i = \frac{K_{0.5\%}}{K_i} \quad (11)$$

Where K_i is the secant stiffness, ζ_i is the stiffness degradation factor, $P_{i,max}$ and $d_{i,max}$ are the maximum lateral load capacity and corresponding displacement during the first cycle at “i%” drift ratio, and $K_{0.5\%}$ is the initial secant stiffness.

4.8. Re-centring capacity and residual drift

While in seismic-resistant design the main focus used to be only on the overall safety, the emerging resilient-based design philosophy has put forward other objectives such as functional recovery, motivated by the desire to minimise financial losses associated with impracticable repair costs. The functional recovery of a building may be assessed by looking at the level of residual deformation suffered by the structure.

Fig. 21 shows the re-centring capacity (RCC) determined by equation (12). The results reflected a rapid surge in the re-centring capacity of the joints during the early stages of loading up to 0.02-0.03 rad, followed by a general plateau in the positive loading direction, with more obvious reductions observed on the opposite side. Overall, the HSS bolts performed slightly better at larger drift ratios, while the self-centring effect due to the superelasticity of the SMA studs was evident in specimens IMJ01-03 during the lower amplitude cycles, which registered generally higher re-centring capacities from the start.



The residual drift ratio, θ_{res} , was obtained by equation (13). Fig. 22 shows the residual drifts plotted against the applied drift ratios in each loading direction, with indicative damage states (DS) defined by FEMA P-58-1 [45] overlaid for reference. The results of the specimens were comparable up to 1% applied drift ratio, with residual drifts generally below the limit of 0.2% (DS1) in the negative loading direction, requiring no re-alignment. Up to 2% applied drift ratio, the residual drifts were below or slightly fluctuating near the 0.5% limit (DS2), indicating that the specimens may only require realignment without the need for structural repairs. During the low amplitude drift ratios, specimens IMJ01-03 recorded lower residual drifts, reflected also by the higher re-centring capacity, owing to the superelasticity effect of the SMA studs which was highly evident particularly in specimen IMJ03. The remarkably low residual drifts of IMJ03 in the negative loading direction may also be attributed to a higher pretension achieved when manually tightening the stud due to its smaller size. Between 3% and 4% applied drift ratio, specimen IMJ06 outperformed the others in terms of reduced residual drift, emphasising the favourable effect of stiffer intra-module connections designed to perform elastically and larger bolt diameters on the re-centring ability. Above the 1% residual drift limit (DS3) the major realignment required to restore the safety of the building may render the structural uneconomical or unpractical to repair.

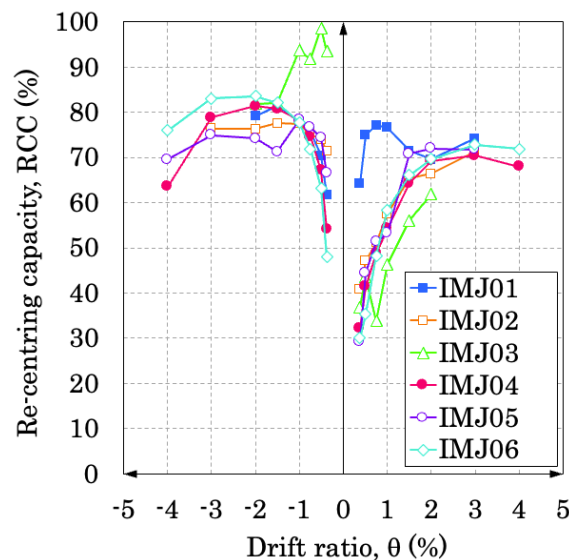


Fig. 21. Re-centring capacity curves.

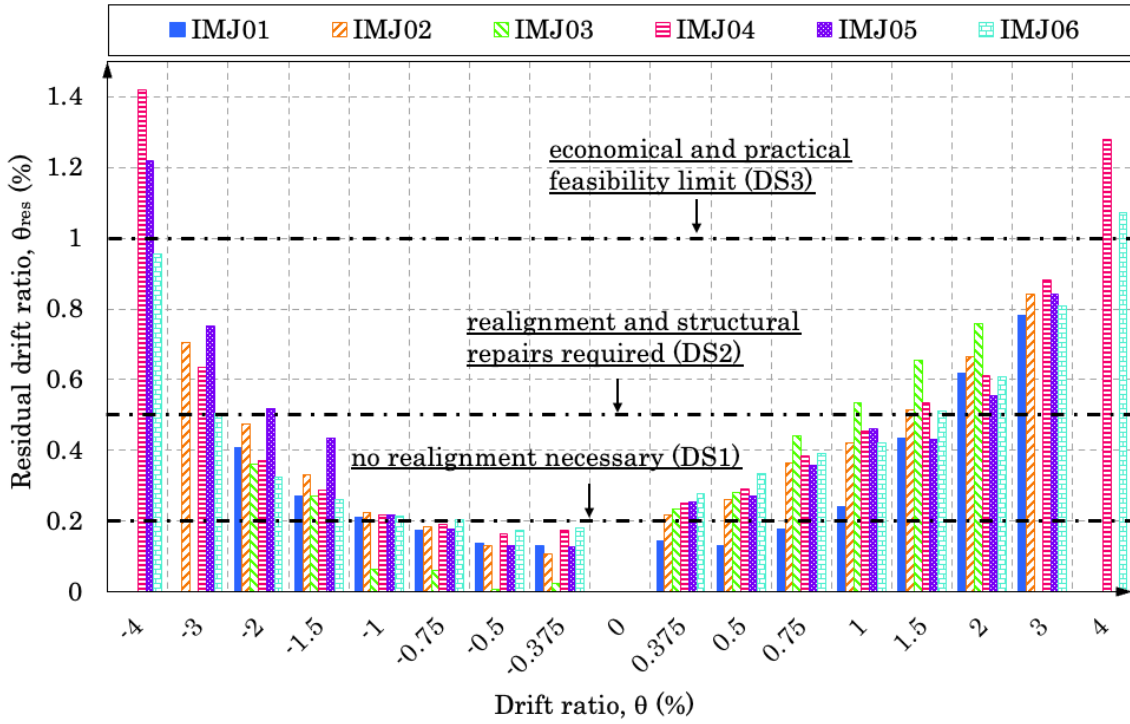


Fig. 22. Residual deformation levels.

$$RCC_i = \left(1 - \frac{d_{i.res}}{d_{i.max}}\right) \times 100 \quad (12)$$

$$\theta_{res} = \frac{d_{i.res}}{H_{storey}} \times 100 \quad (13)$$

Where RCC_i is the re-centring capacity, $d_{i.res}$ is the residual displacement measured at the point of lateral load reversal during the $i\%$ drift ratio cycle, $d_{i.max}$ is the maximum displacement reached in that loading direction during the same cycle, θ_{res} is the residual drift ratio, and H_{storey} is the total height of the specimen (2,750 mm).

4.9. Energy dissipation capacity

The seismic performance of the hybrid joints was further evaluated based on the ability of the specimens to dissipate the input energy during the cyclic lateral loading. Fig. 23 shows the total energy dissipated in the first cycle, E_D , at each drift ratio level, represented by the area enclosed by the hysteresis loops. The reduced values up to 2% drift ratio confirmed the limited inelastic deformation of the frame members up to this level, indicating that the samples were still within the elastic stage. The sudden spike in the energy dissipated during the 3%-4% drift ratios was mostly attributed to the late activation of the frame members hysteresis, which was also reflected by the strain response.



Another method of evaluating the energy dissipation capacity is by the equivalent viscous damping coefficient, ξ_{eq} , obtained by equations (14) - (16) adapted from Chopra [46]. Fig. 24 illustrated the variation of ξ_{eq} at different drift ratios, showing significantly higher equivalent viscous damping coefficients during the early stages, followed by a progressive decrease and a slight recovery after the 2% drift ratio level. This finding was quite unique when compared to the variation of the equivalent viscous damping, provided by steel yielding mechanisms, which usually starts close to zero followed by a steady increase with the progression of the cyclic loading. The remarkable behaviour of the hybrid joints was attributed to the activation of the rubber bearings during the early stages of loading and in particular to the mechanical properties of the high-damping rubber compound used in the rubber layers, while the recovery after the 2% drift ratio was correlated with the delayed influence of the steel frame elements during the third stage of deformation observed on the hysteresis loops.

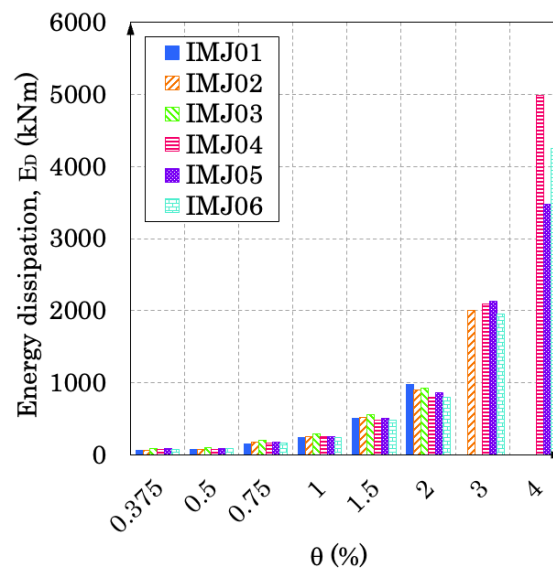


Fig. 23. Energy dissipation capacity.

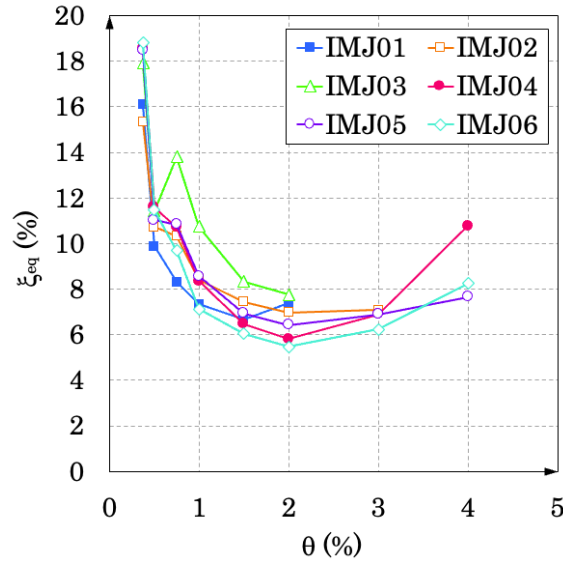


Fig. 24. Equivalent viscous damping coefficient.

$$K_{i,ave} = \frac{|P_{i,max}^+| + |P_{i,max}^-|}{|d_{i,max}^+| + |d_{i,max}^-|} \quad (14)$$

$$E_S = \frac{1}{2} K_{i,ave} \left(\frac{|d_{i,max}^+| + |d_{i,max}^-|}{2} \right)^2 \quad (15)$$

$$\xi_{eq} = \frac{E_D}{4\pi E_S} \times 100 \quad (16)$$

Where $K_{i,ave}$ is the averaged secant stiffness at the i % storey drift, E_S is the area of the averaged equivalent linear response, and E_D is the total energy dissipated in the first cycle at each drift ratio level.

5. Strain response and back analysis verification of test results

The strain vs. displacement curves reflected the seismic response of the hybrid joints from a material level perspective, illustrating the distribution of effort between the framing members of the joint. The yield strain was taken as the average of the yield strain results reported in Table 2, while the nominal yield strain based on nominal EC3 material properties was also given for reference. Due to operational issues during the tests on specimens IMJ01, IMJ03, and IMJ04, the readings from gauges SG01, SG04, SG07, and SG10 were not available. Nevertheless, it was reasonably simple to predict the outcome of the missing readings to a practical extent, based on the repetitive data available from the other tests. As shown in Fig. 26 and Fig. 27, the beams and columns of the specimens with SMA studs were well below the yield limit at the moment of the studs' failure,



allowing the beam-column sub-assemblages to be reused for the tests with HSS bolts as previously explained in Section 3.1.

In general, Fig. 26 showed the expected strain distribution in the beams, with larger values in the top and bottom flanges of the hollow profiles and almost negligible strain levels near the neutral axes (SG04 and SG07). Up to 3% drift ratio, the beams strain values were less than 50% of the yield strain in all specimens, oscillating around 2000 microstrains. Unsurprisingly, the outer flanges in the two beams (SG03 and SG08) recorded higher strains than the inside flanges (SG05 and SG06), attributed to the increased stresses in the rigid regions closest to the intra-module connection. Moreover, the presence of stiffeners at the beam-column joint resulted in a steeper increase of the strains, observed after the 3% drift ratio level, confirming the greater influence of the intra-module connections stiffness on the cyclic behaviour of the IMJs during the third stage of deformation. Also, when compared to IMJ05, the larger diameter of the HSS bolt in specimen IMJ06 prevented the yielding of the bottom flange of the ceiling beam (SG03) in the negative loading direction.

Similarly, Fig. 27 showed that the column strains fluctuated below the yield strain up to 4% drift ratio, with the notable exception of IMJ06 in which the inside flanges yielded at the 4% drift ratio in the negative loading direction. However, it was noticed that the strains of the outside flanges of the column (SG01, SG10) were generally lower than the strains of the inside flanges (SG02, SG09). The higher strain values were attributed to the effect of the two stiffener plates which created a highly stressed region at the location of these strain gauges (SG03 and SG08), suggesting that the actual stress levels recorded on the inside flanges of the beams and columns may have been lower. This observation was supported by the results of IMJ04 which did not have stiffeners at the beam-column connection, exhibiting comparable strains between both sides of the beam and column flanges in both loading directions.

The higher inelastic strains observed in specimens IMJ05 and IMJ06 showed that increasing the strength and stiffness of the hybrid connection causes larger efforts developed in the volumetric frame. Hence, the effectiveness of the proposed connection requires a fine balance between the design of each component in order to ensure the hybrid IMC can resist the forces transferred between the modules, without fully engaging the volumetric module early on and damage its framing elements beyond practical repairability.



Overall, the strain results supported the damage control capability of the hybrid connection, which effectively minimised the effort in the connecting members of the joint. This was mainly attributed to the multi-stage mechanical response of the joints characterised by a sequential activation of the connection components at different deformation levels, delaying the full contribution of the steel frame members until the large amplitude cycles. It must be noted that the current assessment was based on the yield strain determined from the steel coupon tests. When compared to the yield strain from nominal material properties of S355 steel (ca. 1690 microstrains), it may be judged that the yield of the beams and columns occurred between the 2% and 3% drift ratio levels, highlighting the need for careful consideration of overconservative design values when selecting the steel grade to meet the desired yield strain limit in the volumetric module.

To check the validity of the test results, the back analysis was conducted based on the strain gauge readings at maximum lateral load capacity and the comparisons were summarised in Table 8. The results reflected a good overall agreement between the internal forces from the test loads and those obtained from the recorded strains, with some exceptions attributed to the difference between the idealised connection behaviour and its localised mechanisms which cannot be fully explained.

The bending moments developed in the frame elements during the tests were also compared with the predicted resistances of each member in Table 9. The low utilisation ratios in the specimens reflected that the joint members of specimens IMJ01-03 were still in the elastic stage at the failure of the SMA studs, while the yield limit was reached in the bottom column of specimens IMJ05 and IMJ06 at 4% drift ratio, demonstrating the need for thicker or larger sections in the columns of the volumetric module to avoid undesirable failure in the vertical members.

$$M_{tc} = P(H_{tc} - h_{fb}/2) + Nd_{fb} \quad (17)$$

$$M_{bc} = P(H_{bc} - h_{cb}/2) + Nd_{cb} \quad (18)$$

$$M_{fb} = (PH_{tc} + N(\Delta_h - d_{fb}))/ (1 - h_{tc}/2L_b) \quad (19)$$

$$M_{cb} = (PH_{bc} + Nd_{cb})/ (1 - h_{bc}/2L_b) \quad (20)$$

$$\theta_{fb} = M_{fb}/(3EI_{fb}) \quad (21)$$

$$\theta_{cb} = M_{cb}/(3EI_{cb}) \quad (22)$$

$$M_{strain} = E\varepsilon_{test}W_{el} \quad (23)$$

$$M_{el} = W_{el}f_y \quad (24)$$



Where M_{tc}^{test} , M_{bc}^{test} , M_{fb}^{test} , M_{cb}^{test} are the bending moments in the frame members at the location of the strain gauges, P is the lateral load recorded at the top of the specimen, H_{tc} is the distance from the centreline of the floor beam to the level of the horizontal actuators, H_{bc} is the distance from the bottom pin to the centreline of the ceiling beam, L_b is the distance from the centreline of the columns to the pinned roller supports, h_{tc} , h_{bc} , h_{fb} , and h_{cb} are the cross-sectional depths of the frame members as shown in Fig. 25, Δ_h is the equivalent lateral displacement applied at the top of the column, d_{fb} is the horizontal displacement recorded at the level of the floor beam by potentiometer T01, d_{cb} is the horizontal displacement recorded at the level of the ceiling beam by potentiometer T02, θ_{fb} and θ_{cb} are the rotations of the floor and ceiling beams, I_{fb} and I_{cb} are the second moments of area of the floor and ceiling beams, E is the Young's modulus of the steel members, M_{strain} is the equivalent bending moment calculated using the strain recorded during the test, ϵ_{test} is the strain recorded during the test, W_{el} is the elastic section modulus of the steel members, M_{el} is the elastic design resistance of the members, and f_y is the yield strength of the steel members.

Table 8. Comparison of bending moments in IMJ frame members.

Specimen	Load dir.	P_{test} (kN)	M_{tc}^{test} (kNm)	M_{tc}^{strain} (kNm)	M_{bc}^{test} (kNm)	M_{bc}^{strain} (kNm)	M_{fb}^{test} (kNm)	M_{fb}^{strain} (kNm)	M_{cb}^{test} (kNm)	M_{cb}^{strain} (kNm)
IMJ01	(+)	51	56	51	57	50	59	70	59	55
	(-)	52	55	51	57	46	59	61	59	53
IMJ02	(+)	52	55	66	57	64	58	60	59	59
	(-)	59	63	73	65	58	66	58	67	65
IMJ03	(+)	31	33	28	34	29	35	38	35	29
	(-)	39	41	34	42	30	44	43	44	35
IMJ04	(+)	63	68	49	71	69	72	78	73	73
	(-)	73	78	83	80	55	83	99	83	62
IMJ05	(+)	66	70	55	73	76	74	65	75	57
	(-)	80	86	74	88	98	91	97	91	92
IMJ06	(+)	69	74	81	78	57	78	80	80	80
	(-)	84	91	115	92	103	96	87	95	88

NOTE: P_{test} was the maximum lateral load recorded during the test, M_{tc}^{test} , M_{bc}^{test} , M_{fb}^{test} , M_{cb}^{test} were the bending moments in the frame members at the location of the strain gauges obtained by equations (17)-(20), and M_{tc}^{strain} , M_{bc}^{strain} , M_{fb}^{strain} , M_{cb}^{strain} were the bending moments in the frame members obtained by equation (23), where ϵ_{test} was the strain recorded during the test corresponding to P_{test} .

Table 9. Summary of test results and analytical predictions at peak lateral load capacity.

Specimen	Load dir.	P_{test} (kN)	M_{tc}^{test} (kNm)	η	M_{bc}^{test} (kNm)	η	M_{fb}^{test} (kNm)	η	M_{cb}^{test} (kNm)	η
IMJ01	(+)	51	56	0.58	57	0.70	59	0.48	59	0.58
	(-)	52	55	0.58	57	0.69	59	0.48	59	0.58
IMJ02	(+)	52	55	0.58	57	0.70	58	0.48	59	0.58
	(-)	59	63	0.66	65	0.78	66	0.54	67	0.66
IMJ03	(+)	31	33	0.35	34	0.41	35	0.28	35	0.35
	(-)	39	41	0.44	42	0.51	44	0.36	44	0.43



IMJ04	(+)	63	68	0.72	71	0.86	72	0.59	73	0.72
	(-)	73	78	0.82	80	0.98	83	0.67	83	0.81
IMJ05	(+)	66	70	0.74	73	0.89	74	0.60	75	0.74
	(-)	80	86	0.90	88	1.07	91	0.74	91	0.90
IMJ06	(+)	69	74	0.78	78	0.94	78	0.64	80	0.79
	(-)	84	91	0.95	92	1.12	96	0.78	95	0.94

NOTE: P_{test} was the maximum lateral load recorded during the test, M_{tc}^{test} , M_{bc}^{test} , M_{fb}^{test} , M_{cb}^{test} were the bending moments in the frame members at the location of the strain gauges obtained by equations (17)-(20), and η was the utilization factor calculated as the ratio between the test moment resistances and the elastic design resistance of the element obtained by equation (24).

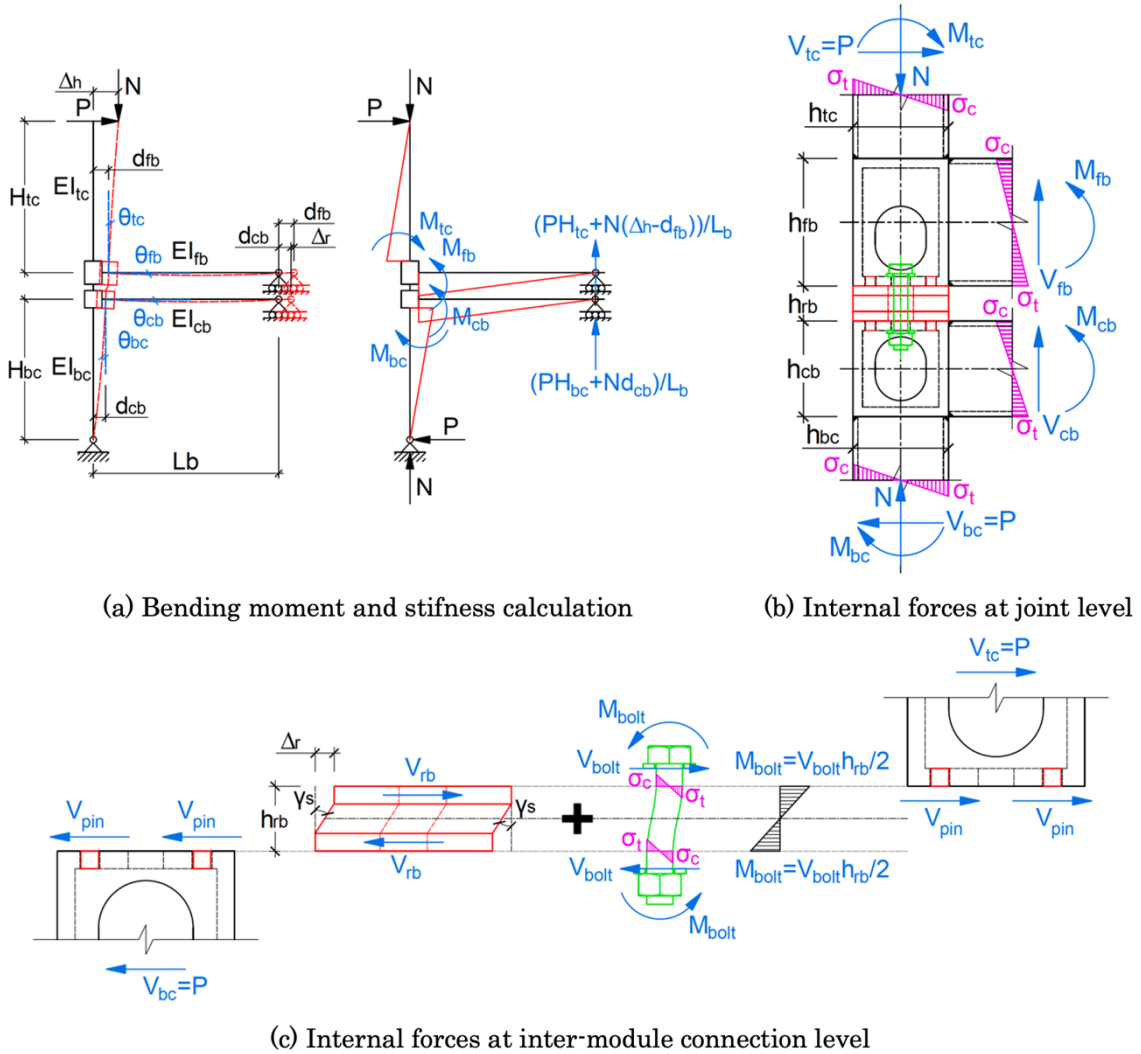


Fig. 25. Mechanical analysis model of the hybrid IMJ.

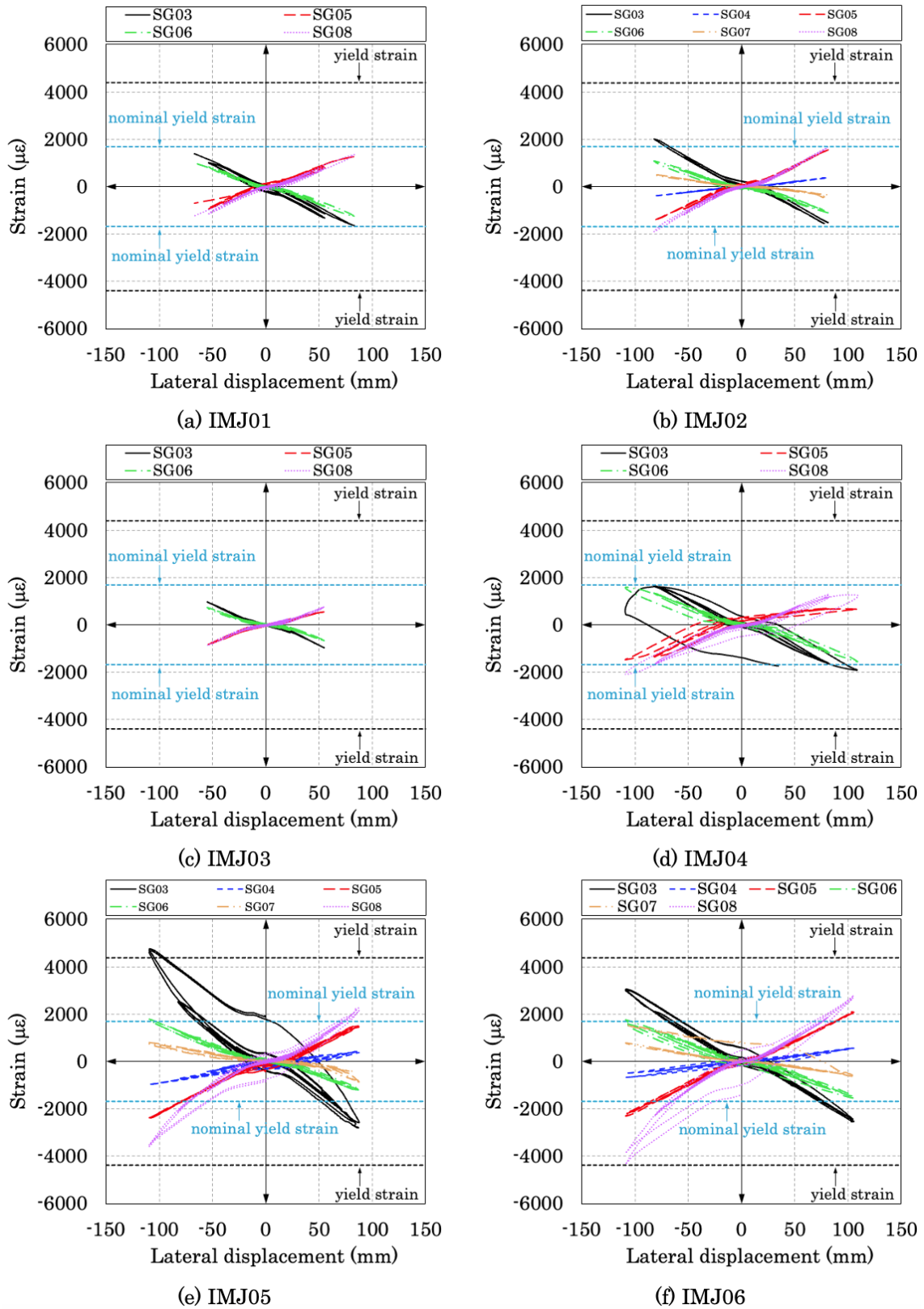


Fig. 26. Strain variation in the ceiling and floor beams.

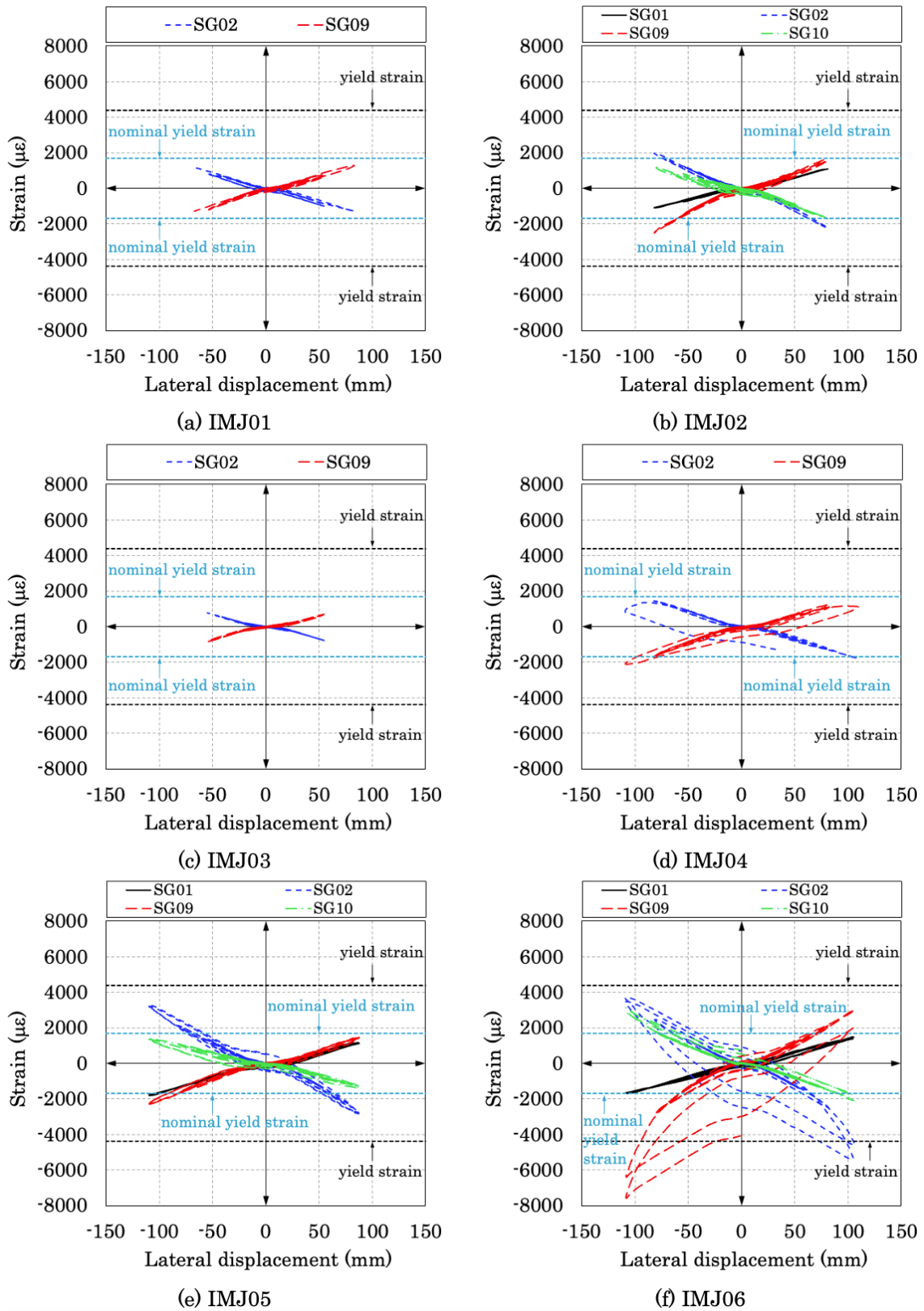


Fig. 27. Strain variation in the top and bottom corner posts.



6. Concluding remarks

A hybrid inter-module connection (IMC) employing a high-damping rubber bearing and a bolting assembly was proposed and previously investigated at connection level through proof-of-concept FEA models. The novel IMC was developed to reduce the permanent damage sustained by the volumetric module after an earthquake through the hybrid force-transfer mechanism harnessed by the rubber bearing. In this study, six inter-module joint (IMJ) prototypes equipped with the novel connection were tested under cyclic loading scenarios to evaluate their aseismic performance and to validate the feasibility of the proposition. SMA studs were introduced to investigate if the superelastic effect of austenitic NiTi would yield meaningful improvements to the re-centring and energy dissipation capacity of the joints when compared to standard high-strength steel (HSS) bolts. The main findings were summarised as follows:

1. The hybrid IMJs exhibited nonlinear hysteretic responses characterised by the sequential activation of different connection components at three different stages. The first stage (up to 0.005 rad) was governed by the low shear stiffness of the rubber bearing, the second stage (0.005 to 0.03 rad) reflected the key influence of the bolting assembly, now fully engaged by the shear deformation in the rubber bearing, while the third stage (0.03 rad and above) highlighted the role of the intra-module connection stiffness.
2. The controlling failure mode of the specimens with SMA studs was the fracture of the Ni-Ti pins, localised away from the threads, at the base of the transition zone, while the HSS bolts survived the full cyclic protocol with noticeable deformation and damage to the threads, without affecting the lateral load capacity.
3. The replacement of the SMA studs after failure uncovered the potential of the bolting assembly as a fuse-like component which could be easily swapped in the aftermath of an earthquake and demonstrated the promising repairability prospects of the connection, supported by the consistent hysteretic responses obtained in the retested specimens. Moreover, the strength reserve observed at the moment of the failures offered valuable insights into the redundancy of the hybrid IMJs.
4. The higher equivalent viscous damping coefficients registered right from the very first stages of deformation emphasised the governing role of the rubber bearing and further proved the effectiveness of the high-damping rubber compound.



5. All specimens exhibited remarkably low residual drifts, below the 0.5% limit up to 2% drift ratio. The overall better results recorded by the SMA specimens illustrated the favourable influence of the superelastic Ni-Ti alloy, yet the difference may not be convincing enough to justify the higher costs compared to the standard HSS bolts. Nevertheless, the falling fabrication costs expected with the rapid advancements in the manufacturing of Ni-Ti parts for civil engineering applications should encourage future efforts in improving the current design.
6. The multi-stage, hybrid mechanical behaviour fostered by the rubber bearing effectively delayed the full participation of the members in the lateral response of the joints, as revealed by the limited inelastic deformation.
7. In the end, the cyclic tests demonstrated the feasibility of the proposed connection with respect to the limitation of damage in the structural elements of the volumetric module after an earthquake, improving the reclaim and reuse potential of the module.

The experimental characterisation of the hybrid IMC has set the benchmark for future work on the validation of high-fidelity FEA models, which will allow further optimisation of the connection components through parametric analyses, while a macro-mechanical model of the hybrid IMC is also being developed to assess the effect of the proposed IMC on the aseismic performance of structures at a system level.

Acknowledgements

This work is funded by the Engineering and Physical Sciences Research Council (EPSRC) in the UK and the industrial partner SC4 (UK) Limited. The authors would also like to thank the Leverhulme Trust (Royal Academy of Engineering) for their initial financial support. Moreover, the authors would also like to express their appreciation to the technical staff in the School of Science & Technology at City, University of London who supported the work in the Heavy Structures Laboratory. The machining and thermo-mechanical treatment of the superelastic SMA studs and material testing of the NiTi alloy was completed at University of Calabria's Department of Mechanical Engineering, Energy Engineering and Management in collaboration with 2SMARtEST Srl (<https://2smartest.com/>), while the laminated elastomeric bearings were fabricated at the Tun Abdul Razak Research Centre (TARRC - <http://tarrc.co.uk>) using a proprietary high damping rubber (HDR) compound.



References

1. United Nations, Department of Economic and Social Affairs. Transforming our World: The 2030 Agenda for Sustainable Development. United Nations; 2015.
2. Gibb A. Off-site Fabrication: Prefabrication, Preassembly and Modularisation. Scotland: Whittles Publishing; 1999.
3. Lawson RM, Ogden RG, Goodier C. Design in Modular Construction. Oxon: CRC Press; 2014.
4. Ferdous W, Manalo A, Sharda A, Bai Y, Ngo TD, Mendis P. Construction Industry Transformation Through Modular Methods. In: Ghaffar SH, Mullett P, Pei E, Roberts J, editors. Innovation in Construction, Cham: Springer; 2022, p. 259–76. https://doi.org/10.1007/978-3-030-95798-8_11.
5. Gunawardena T, Mendis P. Prefabricated Building Systems—Design and Construction. Encyclopedia 2022;2:70–95. <https://doi.org/10.3390/encyclopedia2010006>.
6. McConnell JR, Fahnestock LA. Innovations in Steel Design: Research Needs for Global Sustainability. Journal of Structural Engineering 2015;141:02514001. [https://doi.org/10.1061/\(ASCE\)ST.1943-541X.0001185](https://doi.org/10.1061/(ASCE)ST.1943-541X.0001185).
7. Minunno R, O’Grady T, Morrison GM, Gruner RL. Exploring environmental benefits of reuse and recycle practices: A circular economy case study of a modular building. Resources, Conservation and Recycling 2020;160. <https://doi.org/10.1016/j.resconrec.2020.104855>.
8. Iacovidou E, Purnell P, Tsavdaridis KD, Poologanathan K. Digitally enabled modular construction for promoting modular components reuse: A UK view. Journal of Building Engineering 2021;42:102820. <https://doi.org/10.1016/j.job.2021.102820>.
9. Sajid ZW, Ullah F, Qayyum S, Masood R. Climate Change Mitigation through Modular Construction. Smart Cities 2024;7:566–96. <https://doi.org/10.3390/smartcities7010023>.
10. Lacey AW, Chen W, Hao H, Bi K. Effect of inter-module connection stiffness on structural response of a modular steel building subjected to wind and earthquake load. Engineering Structures 2020;213. <https://doi.org/10.1016/j.engstruct.2020.110628>.



11. Rajanayagam H, Poologanathan K, Gatheeshgar P, Varelis GE, Sherlock P, Nagaratnam B, et al. A-State-Of-The-Art review on modular building connections. *Structures* 2021;34:1903–22. <https://doi.org/10.1016/j.istruc.2021.08.114>.
12. Wang Z, Tsavdaridis KD. Optimality criteria-based minimum-weight design method for modular building systems subjected to generalised stiffness constraints: A comparative study. *Engineering Structures* 2022;251:113472. <https://doi.org/10.1016/j.engstruct.2021.113472>.
13. Farajian M, Sharafi P, Eslamnia H, Kildashti K, Bai Y. Classification of inter-modular connections for stiffness and strength in sway corner-supported steel modular frames. *Journal of Constructional Steel Research* 2022;197:107458. <https://doi.org/10.1016/j.jcsr.2022.107458>.
14. Wang Z, Rajana K, Corfar D-A, Tsavdaridis KD. Automated minimum-weight sizing design framework for tall self-standing modular buildings subjected to multiple performance constraints under static and dynamic wind loads. *Engineering Structures* 2023;286:116121. <https://doi.org/10.1016/j.engstruct.2023.116121>.
15. Corfar D-A, Tsavdaridis KD. A comprehensive review and classification of inter-module connections for hot-rolled steel modular building systems. *Journal of Building Engineering* 2022;50:104006. <https://doi.org/10.1016/j.jobe.2022.104006>.
16. Dai X-M, Zong L, Ding Y, Li Z-X. Experimental study on seismic behavior of a novel plug-in self-lock joint for modular steel construction. *Engineering Structures* 2019;181:143–64. <https://doi.org/10.1016/j.engstruct.2018.11.075>.
17. Chen Z, Wang J, Liu J, Khan K. Seismic behavior and moment transfer capacity of an innovative self-locking inter-module connection for modular steel building. *Engineering Structures* 2021;245:112978. <https://doi.org/10.1016/j.engstruct.2021.112978>.
18. Zhai S-Y, Lyu Y-F, Cao K, Li G-Q, Wang W-Y, Chen C. Seismic behavior of an innovative bolted connection with dual-slot hole for modular steel buildings. *Engineering Structures* 2023;279:115619. <https://doi.org/10.1016/j.engstruct.2023.115619>.
19. Yang C, Chen H, Wen H, Wang Q, Zhang B, Ou J. Experimental study on seismic performance of internal cruciform joints of grouting sleeve connection for modular



- integrated construction. *Engineering Structures* 2024;301:117325. <https://doi.org/10.1016/j.engstruct.2023.117325>.
20. Sultana P, Youssef MA. Seismic Performance of Modular Steel-Braced Frames Utilizing Superelastic Shape Memory Alloy Bolts in the Vertical Module Connections. *Journal of Earthquake Engineering* 2018;24:628–52. <https://doi.org/10.1080/13632469.2018.1453394>.
 21. Wu CX, Yang Y, Wu CY, Yang T, Xu X. Research on seismic behaviour analysis of shock absorbing structure and connecting joints of container assembly structures. *Steel Construction* 2019;34:1-8+73.
 22. Jing J, Clifton GC, Roy K, Lim JBP. Seismic protection of modular buildings with galvanised steel wall tracks and bonded rubber units: Experimental and numerical study. *Thin-Walled Structures* 2021;162. <https://doi.org/10.1016/j.tws.2021.107563>.
 23. Sendanayake SV, Thambiratnam DP, Perera NJ, Chan THT, Aghdamy S. Enhancing the lateral performance of modular buildings through innovative inter-modular connections. *Structures* 2021;29:167–84. <https://doi.org/10.1016/j.istruc.2020.10.047>.
 24. Batukan MB, Sanches R, Hashemi A, Mercan O, Fathieh A, Quenneville P. Seismic performance of modular steel buildings (MSBs) equipped with resilient slip friction joints (RSFJs). *Journal of Building Engineering* 2022;47:103881. <https://doi.org/10.1016/j.jobbe.2021.103881>.
 25. Zhang G, Xu L-H, Li Z-X. Experimental evaluation on seismic performance of a novel plug-in modular steel structure connection system. *Engineering Structures* 2022;273:115099. <https://doi.org/10.1016/j.engstruct.2022.115099>.
 26. Wu G, Feng D-C, Wang C-L. *Modularized Suspended Building Structure. Novel Precast Concrete Structure Systems*, Singapore: Springer Nature Singapore; 2023, p. 273–325. https://doi.org/10.1007/978-981-19-6821-1_8.
 27. Corfar D-A, Tsavdaridis KD. A hybrid inter-module connection for steel modular building systems with SMA and high-damping rubber components. *Engineering Structures* 2023;289:116281. <https://doi.org/10.1016/j.engstruct.2023.116281>.
 28. Lindley PB, Gough J. *Engineering Design with Natural Rubber*. 6th ed. Bertford: Tun Abdul Razak Research Centre; 2015.



29. BSI. Metallic materials — Tensile testing - Part 1: Method of test at room temperature. London: BSI; 2020.
30. BSI. Eurocode 3: Design of steel structures - Part 1-1: General rules and rules for buildings. London: BSI; 2015.
31. Gent AN. Engineering with Rubber: How to Design Rubber Components. 3rd ed. München: Hanser; 2012.
32. Speicher MS, DesRoches R, Leon RT. Experimental results of a NiTi shape memory alloy (SMA)-based recentering beam-column connection. Engineering Structures 2011;33:2448–57. <https://doi.org/10.1016/j.engstruct.2011.04.018>.
33. Fang C, Yam MCH, Lam ACC, Xie L. Cyclic performance of extended end-plate connections equipped with shape memory alloy bolts. Journal of Constructional Steel Research 2014;94:122–36. <https://doi.org/10.1016/j.jcsr.2013.11.008>.
34. Maletta C, Sgambitterra E, Furgiuele F, Casati R, Tuissi A. Fatigue properties of a pseudoelastic NiTi alloy: Strain ratcheting and hysteresis under cyclic tensile loading. International Journal of Fatigue 2014;66:78–85. <https://doi.org/10.1016/j.ijfatigue.2014.03.011>.
35. Sgambitterra E, Magarò P, Niccoli F, Renzo D, Maletta C. Low-to-high cycle fatigue properties of a NiTi shape memory alloy. Procedia Structural Integrity 2019;18:908–13. <https://doi.org/10.1016/j.prostr.2019.08.242>.
36. Lacey AW, Chen W, Hao H. Experimental methods for inter-module joints in modular building structures – A state-of-the-art review. Journal of Building Engineering 2022;46:103792. <https://doi.org/10.1016/j.jobbe.2021.103792>.
37. SAC Joint Venture. Recommended Seismic Design Criteria for New Steel Moment-Frame Buildings. Federal Emergency Management Agency; 2000.
38. AISC. Seismic Provisions for Structural Steel Buildings. Chicago: American Institute of Steel Construction; 2022.
39. BSI. Eurocode 3: Design of steel structures - Part 1-8: Design of joints. London: BSI; 2010.
40. BSI. Execution of steel structures and aluminium structures - Part 2: Technical requirements for steel structures. London: BSI; 2018.



41. Chen Z, Liu J, Yu Y, Zhou C, Yan R. Experimental study of an innovative modular steel building connection. *Journal of Constructional Steel Research* 2017;139:69–82. <https://doi.org/10.1016/j.jcsr.2017.09.008>.
42. Sanches R, Mercan O, Roberts B. Experimental investigations of vertical post-tensioned connection for modular steel structures. *Engineering Structures* 2018;175:776–89. <https://doi.org/10.1016/j.engstruct.2018.08.049>.
43. Zhai S-Y, Lyu Y-F, Cao K, Li G-Q, Wang W-Y, Chen C. Experimental study on bolted-cover plate corner connections for column-supported modular steel buildings. *Journal of Constructional Steel Research* 2022;189:107060. <https://doi.org/10.1016/j.jcsr.2021.107060>.
44. Mullins L. Softening of Rubber by Deformation. *Rubber Chemistry and Technology* 1969;42:339–62. <https://doi.org/10.5254/1.3539210>.
45. FEMA. *Seismic Performance Assessment of Buildings, Volume 1 – Methodology, Second Edition*. Washington, D.C: Federal Emergency Management Agency; 2018.
46. Chopra AK. *Dynamics of Structures: Theory and Applications to Earthquake Engineering*. 5th ed. Harlow: Pearson; 2020.